Space-Time Variations in the Earth Radiation Budget

by
David Lewis Randel

Department of Atmospheric Science
Colorado State University
Fort Collins, Colorado

Spring 1983

Paper No. 374

SPACE-TIME VARIATIONS
IN THE
EARTH RADIATION BUDGET

by

David Lewis Randel

Department of Atmospheric Science
Colorado State University
Fort Collins, Colorado 80523

Spring, 1983

Atmospheric Science Paper No. 374

ABSTRACT

Earth radiation budget data from the Nimbus-7 satellite were analyzed for the period November, 1978 through October, 1979. Results from the narrow field of view (NFOV) scanning radiometers are emphasized but data from the wide field of view (WFOV), non-scanning radiometers will also be presented. The annual cycles of albedo emitted flux and NET radiation are presented showing distinct differences in the albedo cycles from the WFOV and NFOV instruments.

Plots of the zonal averaged radiation budget are included as well as these of zonal averaged annual range. The range plots show large hemispheric differences in annual variability of radiation budget parameters.

The NFOV scanner measured higher albedo and lower emitted flux in areas of extensive cloudiness while in clear subtropical areas lower albedo and higher emitted flux was sensed. This produced higher gradients between the tropics and subtropics (5% albedo, 20 W/m^2 emitted flux) then seen in the WFOV data. Regional areas of abnormal variability in the radiation budget are defined and from studying the yearly cycle of these regions, the causes for the variability are inferred.

Whereas previous WFOV data in the historical record required nearly one week for earth data coverage, the Nimbus NFOV scanners data population is much improved resulting in many cases in total earth coverage accomplished each day. This made possible the study of daily changes in the ERB on a global scale. Daily radiation budget components are examined in extreme blocking situations over the northern hemisphere and are found to show radiation anomalies reaching from high latitudes well into the tropics. A study of the radiation anomalies created by a synoptic cyclone and the 1979 September hurricanes Frederic and David are also presented.

David Lewis Randel
Department of Atmopsheric Science
Fort Collins, CO 80523
Spring, 1983

ACKNOWLEDGMENTS

The author thanks his advisor, Dr. Thomas H. Vonder Haar, for encouragement and guidance of this study. Thanks also to Dr. Thomas B. McKee, a member of the author's committee, Mr. Philip Durkee for advice and many helpful discussions, and Mr. Eric Smith for many of the topic ideas. Mr. Paul Ciesielski and Dr. G. Garrett Campbell provided many of the basic data reading routines. Lastly, the author wishes to thank his parents, Wilton and Verna Randel for over 25 years of patience and support.

This research was sponsored by the National Aeronautics and Space Administration under grants NAS5-27-256, NAS1-16465 and NAG1-150.

TABLE OF CONTENTS

LIST OF TABLES

LIST OF FIGURES

LIST OF FIGURES (cont.)

LIST OF FIGURES (cont.)

Page

1.0 INTRODUCTION

Calculations of the Earth Radiation Budget (ERB), the incoming and outgoing radiant energy were often made (London, 1957) before an accurate method of measurement was derived. These were theoretical calculations based on a number of techniques including measurements of earth albedo from earthshine on the moon. It was not until the advent of artificial satellites in the late 1950s that a platform was provided for instruments that could measure the ERB on a global scale. For the first time it became possible to accurately derive the radiation balance of the earth-atmosphere system.

$$N = (1 - \alpha) Q - I$$

Where N is the net radiation, α the albedo, Q the incident solar radiation, and I the emitted infrared flux. The incident radiant energy originates at our sun and provides approximately 1370 W/m^2 at the top of the atmosphere. The study of this energy's effect on the earth-atmosphere system covers many fields including studies of the ERB and atmospheric energetics. We know the atmosphere works as a great 'heat engine' with the differential heating of the equatorial and polar regions providing potential energy for the system. This energy drives the atmospheric and oceanic circulations by the conversion of potential to kinetic energy. Thus to understand the operation of the atmosphere and oceans we must explain the distribution of the incident radiant energy.

On the average 30% of the incident radiation is reflected back into space. Of the total measured top of the atmosphere reflected shortwave radiation 33% is from the earth's surface and clear sky reflectance. The remaining 66% comes from reflectance by clouds (Wallace and Hobbs, 1977). With nearly 50% global cloud cover it is easy to understand why the location of this high reflectivity surface accounts for the greatest variability in the ERB outside of the differential heating effect. To understand the ERB on regional scales it becomes imperative to know the earth's cloud climatology and what localized radiative effects the clouds produce. Later in this paper areas of high annual variability for each of the ERB parameters are defined and the annual cycles of these areas examined. This is an effort to discover areas with abnormal radiation budget caused by strong cloud/no cloud influences.

The need for accurate ERB information comes from many disciplines and has been the driving force behind the successful radiation monitoring program over the last 20 years. To understand the reasons for climate change on the regional and global scales, answers to many problems are needed. How great is the variability in the sun's output? How does cloudiness of a region effect the radiation budget globally? Does the atmospheric circulation change globally, and what are the causes of this change? Where does the major atmospheric energy transport occur? What role does the ocean energy transport play? What is the annual variability in the ERB? How does ocean energy storage effect the annual variability? Accurate radiation budget data is required to answer these and many of other questions.

With the advent of the computer,.numerical simulation of the earth-atmosphere system has become possible. From the crude measurements of zonal energy balance models of Budyko, Sellers, North, and others came the need for accurate measurements of zonal temperature gradients and fluxes. The first ERB instruments were low resolution sensors that attempted to provide total earth coverage with a minimum of detail, exactly what was needed to validate the simple models. With the advent of more sophisticated general circulation models (GCMs), there became a need for data on regional scales and with higher temporal resolution. Seasonal data, even monthly data became important due to the GCMs requirements for accurate initialization and confirmation data at different times in the model year. Due to the many hundreds of degrees of freedom in the models, the most difficult work with GCMs is understanding the cause and effect relationships of any input parameters. This problem can be lessened if checks are made during the model run with real data, thus the need for a higher temporal scale data.

The emperical calculations of the ERB were accomplished with rather simple radiative transfer models. Since 1970, with the results from the Nimbus satellite series, it became possible to measure the ERB much better than could be calculated. The first attempt to measure the ERB from satellites occured in 1959 with the famous Suomi ping-pong radiometers (Vonder Haar and Suomi, 1971) onboard Explorer 7. This instrument as well as the later flat-plate radiometers provided only crude spatial resolution but were the forerunners of the more advanced hemispherical radiometers (Experimental, ESSA3, ESSA7, Nimbus 2). Vonder Haar's (1968) results from these wide-field-of-view (WFOV) instruments showed the earth to have a lower albedo and a warmer radiative temperature then from concurrent theoretical calculations.

Nimbus 2 (1966) and Nimbus 3(1969) flew instruments that were quite different from the plate detectors. These were scanning radiometers with a narrow-field-of-view (NFOV) spacial resolutions of 200 x 200 km. The data processing for these sensors used complicated bidirectional reflectance models to calculate the top of the atmopshere albedo, and limb darkening models to calculate the emitted radiances (Raschke, Bandeen, 1970). These results showed the earth albedo to be 29-31%, and the effective emitting temperature of 255° K. Unfortunately the scanners data tape recorders failed after only a few months thus stopping data transmission. By 1970 we had almost five years of radiation measurements from satellites. Results from these years presented by Vonder Haar and Suomi (1971) included global maps for each radiation budget component. Using these and other data, Vonder Haar (1972) reported on the natural variability in the ERB over different temporal scales, thus giving the climate modelers an idea of the annual variability inherent in the earth-atmosphere system. Nimbus 3 results from well calibrated broadband and narrow spectral band instruments were presented by Raschke et al. (1973). Zonal averaged radiation budget data for 29 months from 1964-1971 was presented by Ellis and Vonder Haar (1976) showing the changes in ERB for each month of the year.

The early 1970s were a time of improved instrument design culminating in the launch of Nimbus 6 in 1975. This ERB package included both scanning and non-scanning radiometers. Campbell and Vonder Haar (1980) presented results from two years of data from only the non-scanner because unfortunately, the scanning instrument failed after one month with very little data taken. Stephens, et al. (1981) reported on a composite of 48 months of ERB data which included Nimbus

6. They reported an emitted infrared flux of 234 W/m^2 and a planetary albedo of 30%. Nimbus 7 was launched in 1978 and carried an almost identical ERB instrument package as Nimbus 6. The major difference was a cavity radiometer included to measure the total solar flux (Vonder Haar, et al., 1981).

Since Suomi's earliest results the spatial and temporal resolution of ERB sensors has steadily increased. Each new instrument package has been designed to sense more detail and with better accuracy the components of the ERB. With data from the Nimbus 7 scanner we can study broadband measurements from a well calibrated instrument on the regional scale (4.0^o resolution), and at daily time scales. The processing and use of this data is the next logical step in Earth Radiation Budget science.

Large differences in the ERB measurements from the NFOV and WFOV instruments are evident. These differences come from two sources; first, the improved resolution of the scanning radiometer causes higher localized values and larger gradients, second, there are differences in the data processing that could account for any absolute variation. It is nearly impossible to separate these two error sources which have an especially great effect on the albedo data. The scanning radiometer shortwave radiance measurements must be used along with a complicated directional reflectance model to calculate the total reflected energy flux. Introducing this processing to the NFOV data causes many potential errors in the final absolute albedo value, and due to this, less confidence should be placed on the reported NFOV albedo data values. However due to the scanner's higher spacial resolution which produces more detail and larger radiation gradients, the relative values of the NFOV data are assumed to be closer to the actual observed field. Jacobowitz, et al., (1983) discusses the calibration procedures and errors sources for all the Nimbus 7 ERB channels.

Results from the first year data measurements (11/78 - 10/79) including that from both the scanning and non-scanning instruments will be presented. As is consistent with the title of this paper, results from many time and spacial scales are included, but due to the uniqueness of the scanning instrument data, emphasis will be placed on the regional and local space scales. Table 1 is a guide to different scale results presented, and their location within this paper.

Table 1
Location of Different Scale Results

	Annual	Monthly	Daily
Global	3.1.1	3.1.2	
Zonal	3.2.1	3.2.2	3.2.3
Regional Local		3.3.1	3.3.2

Included in this paper are the annual radiation budget (RB) maps of albedo, emitted flux and NET radiation. These define the RB for the year November 1978 - October 1979, and continues the ERB data set from previous satellites. Regions of abnormal annual RB variability are presented and from the study of the annual cycles of these areas, the causes for the variability are discussed. The annual cycles of the RB parameters are presented for both the WFOV and NFOV instruments. Distinct differences in the albedo cycles point to data processing differences and errors.

The zonal averaged (ZA) annual RB from both sensors is presented as well as ZA plots of maps of annual range. Also a ZA case study of the RB in a blocking flow versus zonal flow situation is given and shows decreased mid-latitude gradients of IR flux and albedo.

Finally, as a look into what uses might be accomplished with the daily data, the RB parameters are presented over a synoptic cyclone, in an extreme blocking situation, and over two hurricanes.

With a look toward the future, 1984 will see the launch of the Earth Radiation Budget Experiment (ERBE) consisting of three satellites to be flown simultaneously. This will allow for higher resolution data (2° scanner) and diurnal studies. It is with a look toward this experiment that many of the preliminary results and techniques presented here will be aimed.

2.0 BACKGROUND, DATA PROCESSING

2.1 Nimbus-7 ERB Instrument

The Nimbus-7 (N7) satellite was launched from Vandenberg Air Force Base on October 24, 1978. It was positioned into a sun-synchronous, earth-oriented orbit at an altitude of 950 km. The orbital time is 104 minutes with equatorial crossings at local noon (ascending) and local midnight (descending). N7 carried a variety of scientific instruments, their orientation shown in the satellite schematic Figure 1. These include several instruments used in statosphere and mesosphere studies: the Stratosphere and Mesosphere Sounder (SAMS), and Total Ozone Mapping System (TOMS), the LIMB Infrared Monitor of the Stratosphere (LIMS), and the Stratosphere Aerosol Measurement II (SAM II). The Scanning Multichannel Microwave Radiometer experiment (SMMR) was designed to measure sea surface roughness in the hope of improving ship route forecasting. The Coastal Zone Color Scanner (CZCS) is used to measure ocean sediments, biological productive areas (plankton), and most recently to detect concentration of marine aerosols [Durkee, Hindman, Vonder Haar, (1983)]. Results from the Earth Radiation Budget (ERB) instrument package are presented in this paper.

The ERB instrument consists of 22 radiometer channels divided into 3 major sections (Table 2). The first group contains 10 solar channels that are designed to sense different shortwave spectral bands. Included is channel 10C, a conical cavity radiometer designed to accurately measure the total solar flux. Results from 10C for the first two and one-half years of

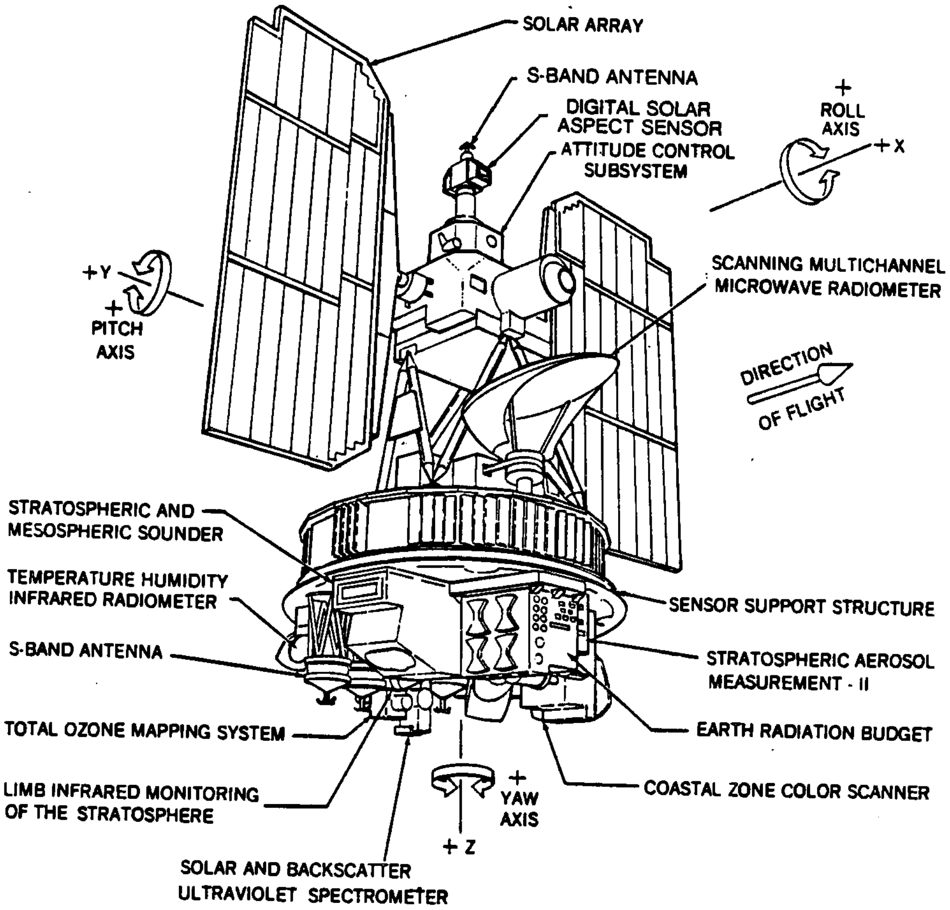

Figure 1. The Nimbus 7 Observatory (From the Nimbus 7 User's Guide).

one-half years of operation are presented in Figure 2, from Hickey, et al., (1982).

Table 2
ERB Channels and Characteristics

Channel	Wavelength Limits (μm)
1	0.2-3.8
2(a)	0.2-3.8
3	<0.2 to>50
4	0.526-2.8
5	0.698-2.8
6	0.395-0.508
7	0.344-0.460
8	0.300-0.410
9	0.275-0.360
10C	<0.2to>50
11	<0.2to>50
12*	<0.2to>50
13	0.2-3.8
14	0.695-2.8
15-18	0.2-4.8
19-22	4.5-50

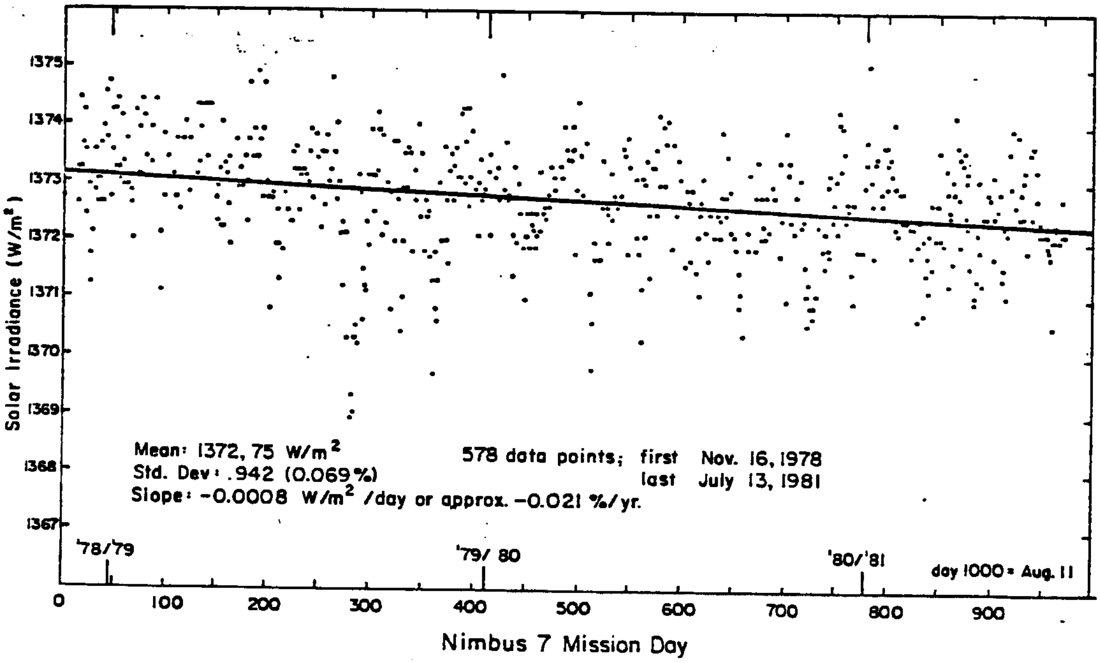

Figure 2. Nimbus 7 ERB Cavity Solar Irradiance Channel 10C.

The second major ERB section includes 4 channels (11-14) of fixed wide angle field of view radiometers. These are thermopile type earth-oriented sensors designed to measure total earth fluxes of long and shortwave radiation. Channel 12 measures the total earth flux, and in conjunction with Channel 13 the longwave flux is calculated.

Longwave = channel 12 - channel 13 [day]
Longwave = 3.8 - >50 μm
Shortwave = .2 - 3.8 μm

The third instrument group includes the scanning radiometers, Channels 15-22. On the 'bottom' of the ERB package is a cylindrical scan head, gimbel mounted, containing four telescopes. This arrangement allows for a change in the direction of the telescopes by rotation of the scan head in .25° steps and the gimbel in .5° steps. Each of the scanning telescopes has a rectangular field of view, .25 X 5.12°. Inside the scanner the telescope beams are split into the shortwave (SW) Channels 15-18, and the longwave (LW) Channels 19-22, thus producing coincident earth data for both LW and SW. When in operation, the scan head is stepped at varying degrees over each half second in an attempt to maintain constant ground resolution of 150 km. Figure 3 gives the patterns of the five different scan modes of which scan mode 5, the normal mode of operation for maximum earth coverage, is repeated every 1400 km along with sub-satellite track. This mode also allows for a maximum number of angular measurements used to derive the characteristic angular distribution models from which the total flux from an area is calculated (Jacobowitz, 1978).

2.2 Earth Radiation Budget Measurement Theory

To measure the Earth Radiation Budget (ERB) from the Nimbus-7 (N7) satellite, two distinctly different approaches and measurement systems

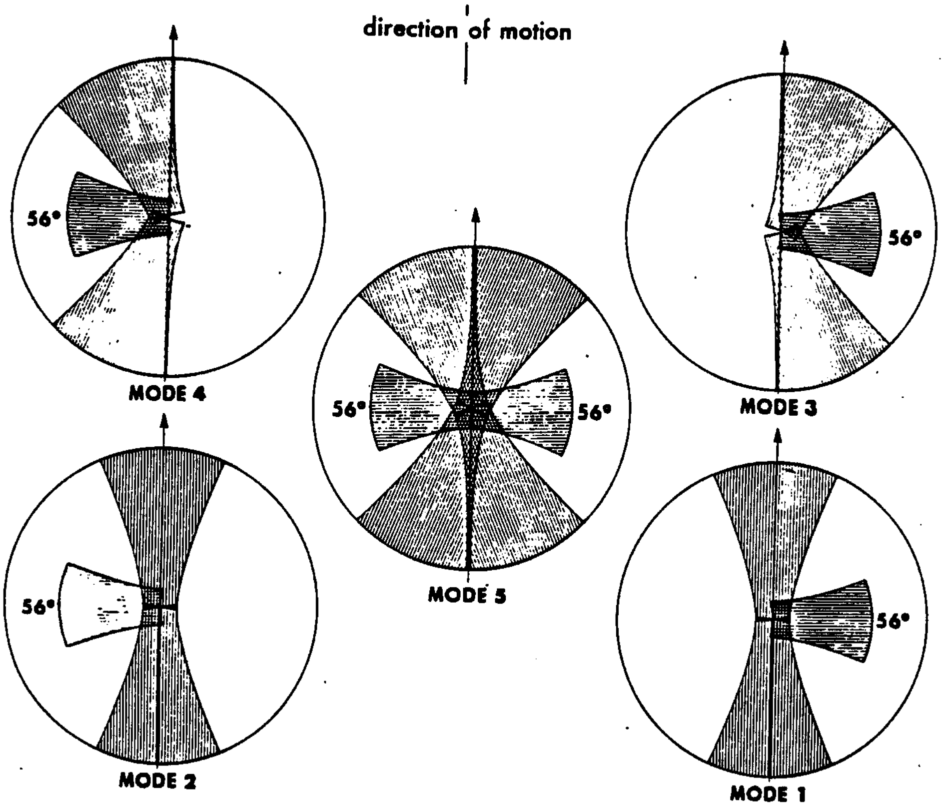

Figure 3. Scan modes of the Nimbus 7 scanning radiometer - scan mode 5 is the normal mode of operation.

are employed. There are the flat plate hemispheric sensors (WFOV), and the scanning (NFOV) sensors. The radiation measurement technique of each type is graphically displayed in Figures 4a and 4b.

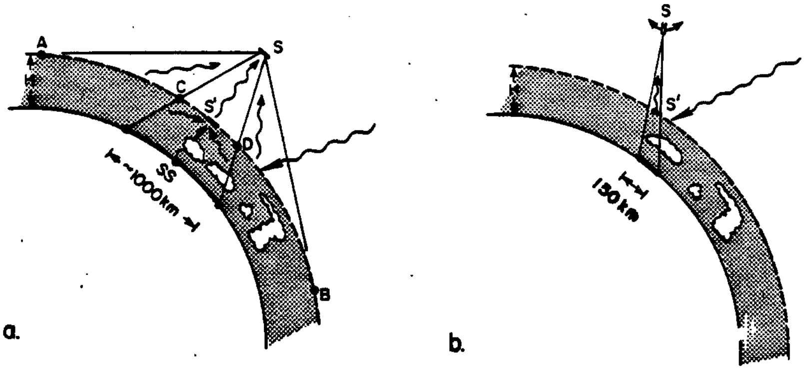

Figure 4. Schematic representation of the measured quantities by a) flat plat WFOV radiometers B) scanning NFOV radiometers (from Stephens, et al. (1981).

Shown in 4a, the flat plate sensors measure the radiant upwelling flux in cone SAB at the satellite point S. The goal is to convert this measurement to the top of the atmosphere flux at height H. The cone SCD is defined by the solid angle corresponding to the half power region of the sensor. This explains why the maximum ground resolution of this type sensor is near 10–15° or greater then 1000 km. The conversion from satellite altitude flux to top of the atmosphere flux to the zero order is by $(r_{sat}/r_{earth})^2$, assuming a point radiation source at the earth's center. Although the WFOV sensors have poor ground resolution, the advantage is they measure the majority of the total flux by using a simple and dependable design.

Shown in Figure 4b is the measurement method of the scanning radiometers (Channels 15–22), improved ground resolution being their major advantage (150 km). The radiance at S', the top of the atmosphere, is rather a simple conversion from the satellite measurement, but due to viewing in a very small finite solid angle, only a small amount of the total radiant exitance is measured. This accounts for the major hurdle with using scanning radiometer data. The calculation of the total emitted infrared flux (I) can be done with relative ease. Near blackbody emissivity can be assumed, and since blackbody radiation is isotropic, the direction problems are eliminated. To determine the albedo of a target area, the angular variation of the data becomes a much more severe problem. A correction must be added to the data that explains variations of radiance with changes in solar zenith, observation zenith, and relative zenith angles. This correction takes the form of a bidirectional reflectance model and includes changes in surface conditions, cloud cover, and cloud type. One of the main goals in analyzing data from the N7 scanner is to gather measurements at many different viewing angles, over the same area, in an attempt to define this model for future experiments. It is only once this correction is added to scanner data, that the total reflectant energy and thus the albedo can be computed. Due to it's complexity the conversion of satellite radiance to top of the atmosphere flux was accomplished at NASA-Langley during the initial data processing. Many changes have been made to the processing schemes which accounted for the delay in producing the finalized fluxes.

The albedo (α) is defined as the percent of the incident solar radiation that is reflected back to space. The incident radiation (Qi) must also be computed for changes in earth-sun distance and solar zenith angle. The solar constant is defined as:

$$S = \frac{Q_s}{4\pi(ES)^2} = 1370\ W/m^2$$

Where Q_s is the radiant flux of the sun, ES the mean earth-sun distance. With correction the incident solar radiation, (the amount received per unit area) is defined as:

$$Q_I = S\ (\frac{ES}{d})^2 \cos Z$$

where d is the instantaneous distance, earth-sun and Z the solar zenith angle.

The albedo, emitted flux and incident solar irradiance were calculated from the satellite radiance values at NASA-Goddard Space Flight Center (GSFC). This accounted for the major part of the data processing that was performed on the data before it was received at Colorado State University. Also included in these calculations, was the computation of the radiation balance, or NET radiation.

$$NET = (1 - \alpha)\ Q_I - I$$

The NET gives a measure of the excess or deficit energy in the system. For the average annual global temperature to remain constant, the annual average of the NET radiation must be zero; there must be as much energy emitted by the system as absorbed. The scanning radiometer data from N7 for 1978-1979 indeed showed a NET radiation of zero within instrument accuracy.

2.3 N7 Data Collection Data Types - NASA-Goddard (GSFC)

Data collection from N7 over the last four years has been remarkably uniform, but due to power requirements of the satellite, the

ERB instrument package is operated on a three days on, one day off cycle. This has various effects on the instruments, but some warm-up period is always needed after power-up before accurate readings can be taken. Also the operation of the scanner has been shown to have localized heating effects on the other ERB instruments. N7 ERB data is archived at GSFC so that each 24 hour period of data plus the satellite orbit parameters are recorded onto a single NASA Master Archive Tape (MAT). For each year there are approximately 275 MAT tapes produced. Data from the ERB instruments is still being collected at GSFC as the WFOV instruments are still functioning although the sensors have degraded due to exposure to solar radiation. A major advantage of the longwave scanning radiometers were their ability to look at internal blackbodies, therefore performing in flight sensor calibration. Unfortunately only 18 months of scanner data was produced due to the scanning mechanism's failure.

For each month of data collected on MAT tapes, one Mapped Data Matrix Tape (MATRIX) is produced (also at GSFC). Data for this paper came from these tapes, which contain world grids of the ERB parameters. To produced the MATRIX tapes, ERB data was sorted into 2070 target areas as a function of geographical area. The latitude resolution of each area is always 4.5°, but to keep the target surface area approximately the same size, the longitude spacing increases with latitude (Table 3).

Table 3
Scanning Radiometer Target Areas

Latitude Limits Lower Limit	Latitude Limits Upper Limit	Longitude Interval*
0.0	4.5	4.5
4.5	9.0	4.5
9.0	13.5	4.5
13.5	18.0	4.5
18.0	22.5	5.0
22.5	27.0	5.0
27.0	31.5	5.0
31.5	36.0	5.0
36.0	40.5	6.0
40.5	45.0	6.0
45.0	49.5	6.0
49.5	54.0	7.5
54.0	58.5	8.0
58.5	63.0	9.0
63.0	67.5	10.0
67.5	72.0	12.0
72.0	76.5	18.0
76.5	81.0	22.5
81.0	85.5	40.0
85.5	90.0	120.0

*For each latitude band the longitude intervals start at the 0 degree meridian and progress east by the increments listed.

For processing the ERB scanning channels, these areas are actually an average of nine collection areas which represent the 150 km resolution of the sensor. For the WFOV instruments which have an effective ground resolution of near 15°, the sorting represents a false increased resolution. Data is presented on the MATRIX tapes in forms other than the 2070 point fields. Included are both Mercator and Polar Stereographic projections for a limited number of parameters. Data fields on the MATRIX tapes include direct measurements, computed averages, and statistics for 37 parameters over 3 different temporal periods. The parameters and the time periods for which they are available are shown in Table 4 (ERB MATRIX tape documentation, 1981).

Table 4
ERB MATRIX Parameters
(D=Daily, C=Cyclic, M=Monthly)

Paramters	Availability	Description
1	DM	Data Population of WFOV Observations - AN
2	DM	Data Population of WFOV Observations - D
3	DM	LW Flux from WFOV Observations - AN
4	DM	LW Flux from WFOV Observations - DN
5	DM	Computed Maximum Reflected Energy (.2-4u) for WFOV - AN
6	DM	Computed Maximum Reflected Energy (.2-4u) for WFOV - DN
7	DM	Computed Maximum Reflected Energy (.7-3u) for WFOV - AN
8	DM	Computed Maximum Reflected Energy (.7-3u) for WFOV - DN
9	DM	Reflected Energy (.2-4u) from WFOV Observations - AN
10	DM	Reflected Energy (.2-4u) from WFOV Observations - Dn
11	DM	Reflected Energy (.7-3u) from WFOV Observations - AN
12	DM	Reflected Energy (.7-3u) from WFOV Observations - DN
13	DM	Earth Albedo (.2-4u) from WFOV Observations
14	DM	Earth Albedo (.2-.7u) from WFOV Observations
15	DM	Earth Albedo (.7-3u) from WFOV Observations
16	DCM	Net Radiation from WFOV Observations
17	DM	SW Data Population of NFOV Observations - AN
18	DM	SW Data Population of NFOV Observations - DN
19	DM	LW Flux from NFOV Observations - AN

Table 4
(continued)

Paramters	Availability	Description
20	DM	LW Flux from NFOV Observations - DN
21	DM	Average LW Terrestrial Flux from NFOV Observations (weighted average of AN and DN data)
22	DM	Earth Albedo from NFOV Observations
23	DCM	Net Radiation from NFOV Observations
24	DM	LW Data Population of NFOV Observations - AN
25	DM	LW Data Population of NFOV Observations - DN
26	CM	Data Population of Averaged WFOV LW Flux
27	CM	Data Population of Averaged NFOV LW Flux
28	M	Averaged LW Terrestrial Flux from WFOV Observations
29	M	Normalized Dispersion of LW Flux from WFOV Observations
30	M	Normalized Dispersion of Earth Albedo (.2-4u) from WFOV Observations
31	M	Standard Deviation of Net Radiation from WFOV Observations
32	M	Normalized Dispersion of Averaged LW Terrestrial Flux from NFOV Observations (Parameter 21)
33	M	Normalized Dispersion of Earth Albedo from NFOV Observations
34	M	Standard Dispersion of Earth Albedo from NFOV Observations
35	M	Minimum Earth Albedo from NFOV Observations
36	M	Average Solar Insolation
37	M	Earth Albedo (.2-4u) from WFOV Observations <u>without</u> Solar Zenith Angle Correction

Most parameters have daily and monthly fields but the net radiation fields from both the WFOV and NFOV instruments have six day averages included. As was mentioned, a major advantage with using the scanning radiometer data is the increased data population (D.P.) that results. The daily D.P. fields are included and indeed show 10-15 observations per day from the scanner compared to 0-4 per day for the WFOV channels.

The MATRIX tapes are 9 track, 1600 bpi and are generated at NASA-Goddard on a IBM 360/91 computer. Twelve tapes of data, (the first year of observations) were received at Colorado State University (CSU) in August, 1982. Using the CDC Cyber 720 system at the University Computer Center, a first look at the data fields was accomplished, and routines originally produced by Garrett Campbell for use with Nimbus-6 data were extensively used. By the use of a contouring routine and a Versatec plotter, plots of any MATRIX field could be output. Secondary and final data processing used the Department of Atmospheric Science computer facility. Included in this system is a DEC VAX 11/780 connected with a Comtal Vision One/20 imaging system. The majority of results to be presented comes from the work on this system. For output of a computed field, three mediums are used. First data can be sent along a network from the VAX 11/780 to the CDC machines for plotting on the Versatec plotter. Second, fields are displayed and enhanced on the Comtal System's color monitor. This was the easiest method due to the fast display procedures and the excellent color graphics that could be produced. Finally the fields, (once they were in Comtal image format) could be copied out to a high resolution Optronics Colorwrite system, which is capable of producing both color negative film and transparencies. Fortran routines were written to read and analyze any

MATRIX field, and many of these procedures will be outlined in the following section.

2.4 Data Processing Techniques - Colorado State University

Each world grid data field on the MATRIX tapes has 2070 points, each point assigned a specific 4.5 latitude by variable longitude area. To look at the actual data, as was done in the regional studies, every point found to have coordinates inside a choosen latitude-longitude is printed out. To perform a subtraction, addition, or division of any two fields, it is only necessary to match up the index of the 2070 point array and the geographical areas also match up. The operation between all points in the field is completed and a resultant 2070 point field is produced. Using this method the difference is found between the ascending and decending infrared flux fields, thus producing the diurnal variation. It was often desired to combine a number of days into a multi-day average, as for comparison with the Monthly Weather Review weekly averaged synoptic maps. This entailed adding up the data from each area over the time period, and dividing by the total number of days for which data was available. This was necessary because many days have wide areas of missing data. For the major ERB parameters, data population fields are included on the MATRIX tapes. Averages calculated for these parameters were weighted by the daily data population from the tapes.

Zonal averages were calculated by averaging all non-indefinite values within each 4.5° latitude band, producing 40 zones between 90° and 90°S. Zonal averages for each ERB parameter were produced for every month and constructed into time series over the months 11/78 - 10/79. For calculation of the global average there are the following steps:

1) calculate the zonal averages (Xj) where j equals all of the 40 latitude zones.

2) weight the zonal average by geographical surface area

$$S_j = (\sin\theta_j + 1 - \sin\theta_j)$$

$$W_j = \frac{S_j}{\sum_{n=1}^{40} Sn}$$

3) sum the weighted zonal averages into the global average

$$GA = \sum_{j=1}^{40} W_j X_j$$

For the albedo field a solar insolation weighting factor must be included in the surface area weighting factor:

$$S_j = S_j \cdot I_j$$

Where I_j is the solar radiation incident of zone j. The hemispheric averages are computed by averaging the first 20 zones for the northern hemisphere and the last 20 zones for the southern. To calculate the annual global averages, the monthly averages for each of the 12 months were combined. To calculate the yearly amplitude or range of a parameter, the 12 monthly fields are read in, the maximum and minimum at each point found, the difference calculated, and the resultant field output. At various points in the data processing checks are made of the data to assure the values stay within an acceptable range. These include albedo 0 - 100%, IR flux 0 - 400 W/m^2, and net radiation -250 to 200 W/m^2. This filtering was found to affect only the data when it was obviously out of reasonable bounds.

Processing on the VAX 11/780 also included several smoothing routines that were used on the output fields to fill in missing data. For individual missing data points, the surrounding four points were averaged and the value filled in. For oceanic areas where the fields showed zonal uniformity, interpolation between good points to each side of the missing point(s) was used. Generally when there were large sections of missing data, or there were missing points over continents with large gradients, no smoothing was used and missing data is evident in the output.

After examining the yearly ERB regional scale cycles, it was decided to remove the first harmonic from the data in an attempt to observe cycles other than that caused by the dominate annual solar cycle. By calculating the Fourier components Am, Bm of the 12 month data series the mth harmonic in the data can be eliminated. Am and Bm are defined as:

$$Am = \frac{2}{L}\int_{o}^{L} f(x)\sin(\frac{2\pi mx}{L})dx$$

$$Bm = \frac{2}{L}\int_{o}^{L} f(x)\cos(\frac{2\pi mx}{L})dx$$

Where L is the total cycle length, m the number of intervals in the cycle, and f(x) the function value at x (the data at month x). The mth harmonic is then calculated as:

$$fm(x) = Am \sin (\frac{2\pi mx}{L}) + Bm \cos (\frac{2\pi mx}{L})$$

To remove the mth harmonic from the data a simple substraction is needed:

$$f_{x-m}(x) = f(x) - f_m(x)$$

To calculate Am and Bm, it was necessary to approximate the integrals over a finite set of data points. Because the cycle most represented a second order curve, Simpsons composite integral approximation scheme was chosen:

$$\int_{o}^{L} f(x)dx = \frac{h}{3}[fx_o + 2\sum_{j=1}^{\frac{L}{2}-1}(fx_{2j}) + 4\sum_{j=1}^{\frac{L}{2}} f(x_{2J-1}) + fx_L]$$

where:

$$\text{Am:}\quad f(x) = x\sin(\frac{2\pi mx}{L})$$

$$\text{Bm:}\quad f(x) = x\cos(\frac{2\pi mx}{L})$$

The components Am, Bm were calculted for each parameter for each point in the field. After removing fm(x) from the data, new regional averages were computed and modified yearly cycles were produced.

To examine and output any data field it was necessary to arrange the data into some kind of map projection. The easiest projection and the one choosen is the 'cylindrical equidistant projection'. The 2070 point fields are expanded to 40 x 80 field by interpolating along longitude data points. Examples of these maps are shown extensively throughout the next section. Major reasons for the choice of this projection are: first, plotting routines on the University Cyber 720 computers were ready to accept data in this form, second, a great percentage of the output was sent to the Comtal Vision One/20 display system. This system can display any size rectangular field easily if it has a constant record length, in this case 80 data points in each latitude zone. The smoothing routines mentioned earlier were constructed to aid the display procedures of this system. Each field to be displayed on the Comtal, must be converted to integer values, eight bits per byte format, thus after conversion the values ranged from 0-255. The Comtal system displays on it's monitor, the data in 255 different gray shades and a color enhancement table can be added to change any gray shade value to any color. This was used for 'quick looks' at the data and was most useful in studying enlarged and smoothed daily data. Color prints, slides, and transparencies were produced on the Optronics Colorwrite system which uses data directly from the disk storage to produce high accuracy, high resolution images.

3.0 Results

3.1 Global Radiation Budget

3.1.1 Annual

Results presented are from the first year Nimbus 7 (N7) ERB data set, from the period November 1978 through October 1979. Emphasis in data processing was placed on the NFOV scanning radiometer data, to provide higher spatial and temporal resolution results. The majority of past data sets were from WFOV instruments, thus in order to discover what new results might be seen in the scanner data, it was important to compare the N7 WFOV and NFOV sensors.

Shown in Figure 5 are the annual NFOV emitted flux (IR flux), and albedo. It is important to note the general reciprocity of the values on each map. Areas where the IR flux is high, representing clear warm regions, are areas that the albedo is accordingly low. The map of annual IR flux, Figure 5a, shows high values in the subtropics off the west coast of continents. These are clear sky areas of supressed cumulus convection in the downward branch of the Hadley cell. There are small areas where this reciprocity is not as evident. An example is the small albedo increase noted directly off the central west coast of South America, in an area dominated by statocumulus clouds. These areas are important due to the anomalies that are created in the NET radiation patterns. With the sensor seeing well into the atmosphere or at the surface the emitting temperature is high, producing high measured values

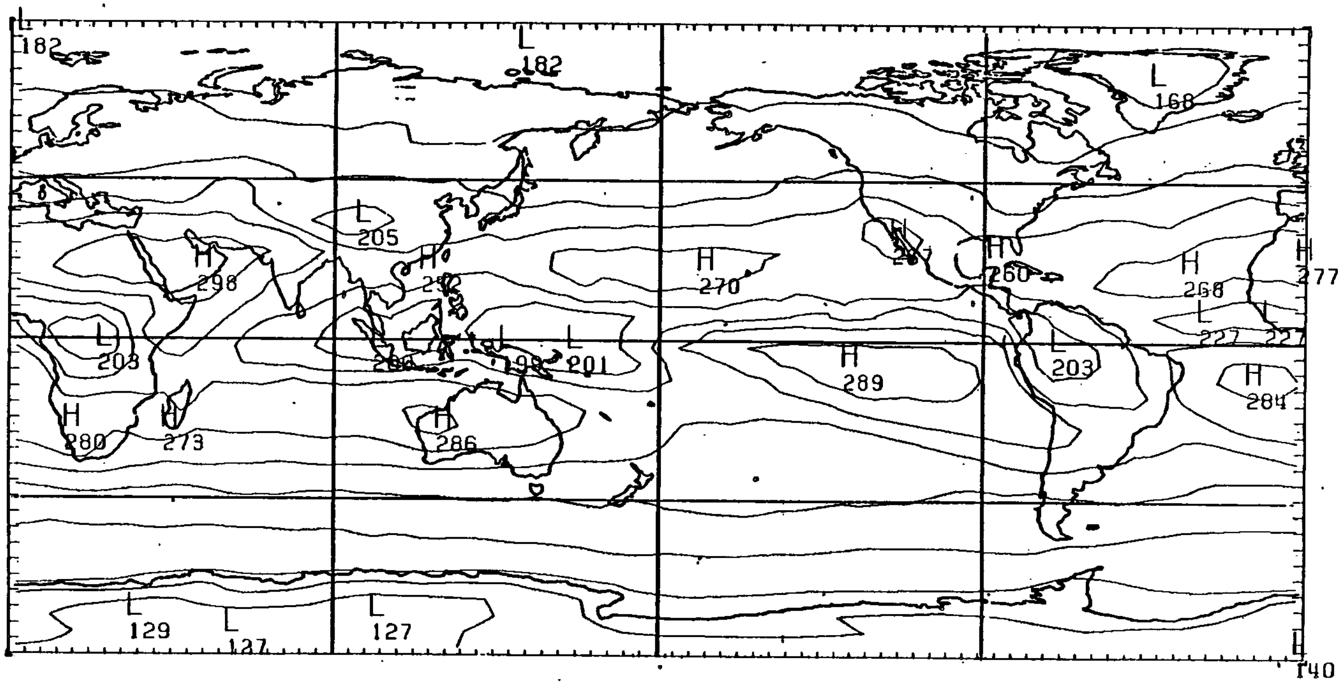

Figure 5a. Annual emitted flux (W/m^2) Nimbus 7 scanning radiometer November 1978 - October 1979.

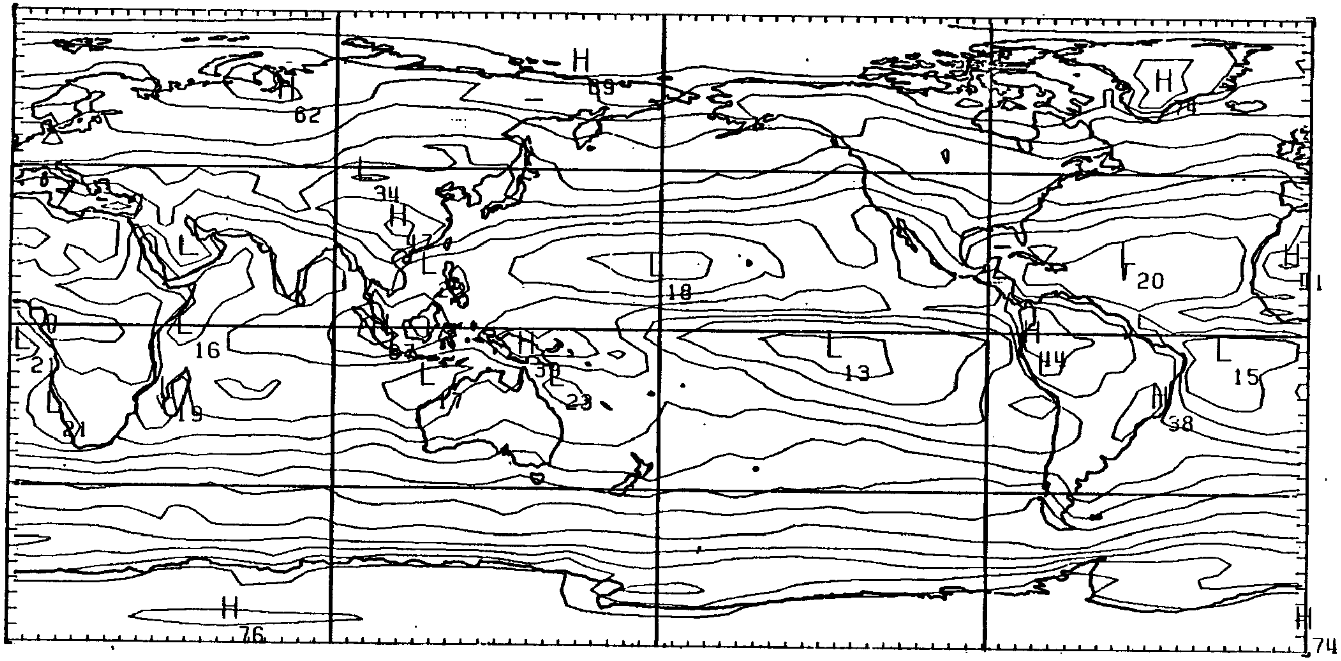

Figure 5b. Annual albedo (%) Nimbus 7 scanning radiometer November 1978 - October 1979.

of IR flux. Regions of tropical cloudiness are characterized by low IR flux values caused by sensing of the cold cloud tops. These areas include the tropical continents of Africa, South America, and the 'island' continent of Indonesia. Low values in the IR flux clearly show the location of the Intertropical Convergence Zone (ITCZ) in both Pacific and Atlantic equatorial oceans. The scanner also has the ability to look away from the sub-satellite track and sense the higher latitude polar regions. Thus the effect of glacier covered Greenland's colder emitting temperature is seen. In Figure 5b the corresponding high albedo areas with low IR flux can be noted. Greenland's albedo of 74% is highly anomalous to other values at that latitude. The low albedo areas off the west coast of continents and of the Mediterranean Sea are clearly seen. The high albedo regions of tropical convection over the continents and the ITCZ, as well as the high values of the Sahara caused by large surface reflectivity are shown. The anomalous high albedo (47%) over the Tibet plateau matches with low IR flux, and is due to the snow covered and barren ground of this high elevation source. The most striking feature of both maps is the strength of the meridional gradients in the tropics. Gradients of 100 W/m^2 emitted flux and 30% albedo are of the same magnitude as those of the Equator-Pole. It is no wonder that strong tropical meridianal circulations are found.

It is often stated that albedo and IR flux are of secondary importance compared to the NET radiation. This is because the NET is a measure of the excess or deficit energy that can be converted or taken from other atmopsheric and/or oceanic processes. The annual maps of NET radiation from both the NFOV and WFOV, Figure 6, show roughly the same pattern. A NET gain is shown in the tropics and a loss above

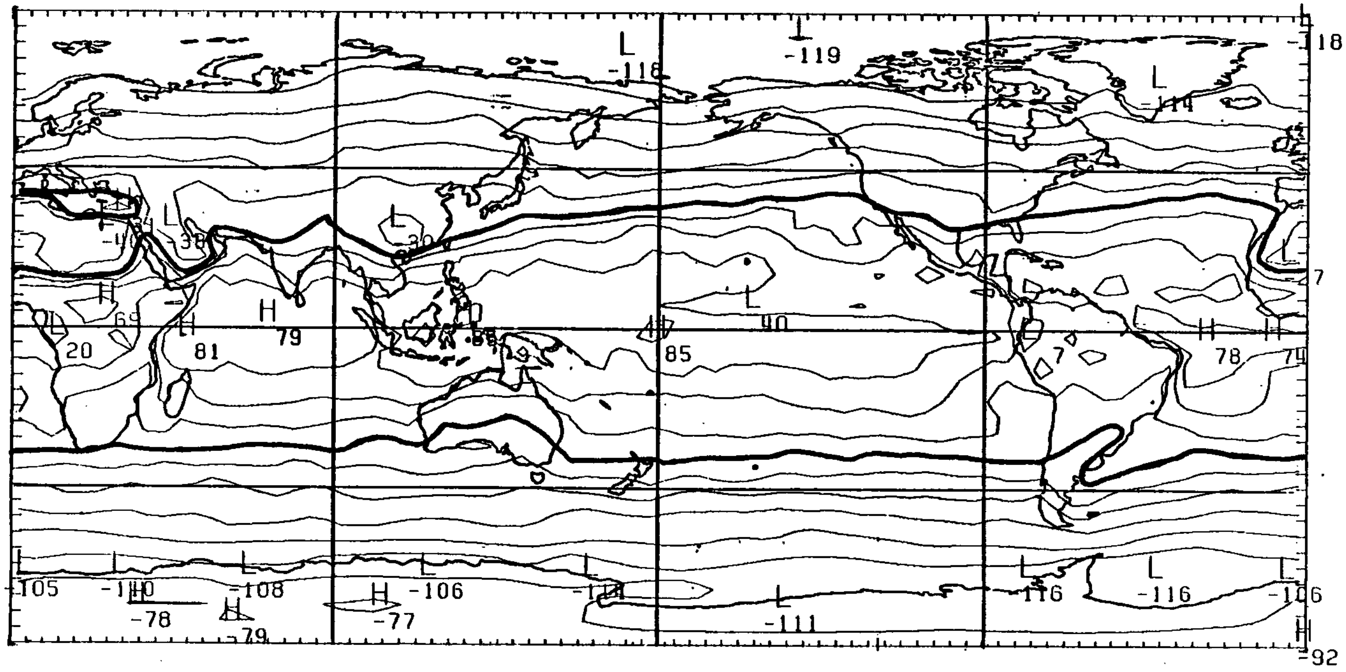

Figure 6a. NET radiation (W/m^2) Nimbus 7 scanning radiometer Novmeber 1978 - October 1979.

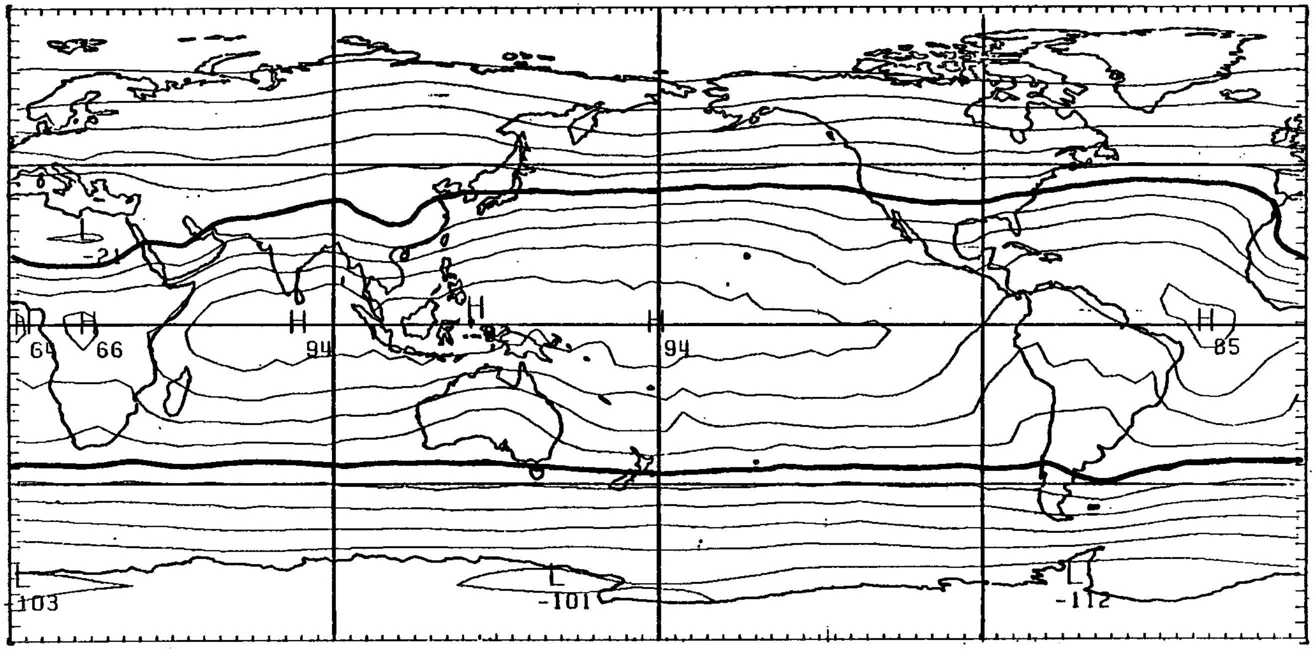

Figure 6b. NET radiation Nimbus 7 WFOV non-scanner November 1978 - October 1979.

approximately 30° latitude. Regions of highest gain are found in low latitude, clear sky areas, and those of greatest loss found in polar regions near the boundary of the summer ice melt. A major anomalous feature is shown in the Figure 6b, the three wave pattern in the southern hemisphere caused by the decreased values over the continents and the west coast statocumulus (Vonder Haar, 1981). It is believed synoptic systems follow these radiation contours, and work is presently underway to validate this hypothesis. In Figure 6a more meridianal features are noted. These include the NET gain over the Mediterranean Sea, and the NET loss over the Tibet plateau, Saudi Arabia, and North Africa. The latitudinal extent of the NET gain area varies widely with longitude. Between 20° west and 45° east longitude, NET loss occurs as far south as 15°north. This large tropics-subtropics gradient is evidence of a strong Hadley circulation, where in the downward branch, the Sahara desert has been formed. Here the NET loss is balanced by the large scale subsidence, thus creating positive feedback for dry conditions (Charney, 1975).

In the previous annual averages the NFOV data showed distinct differences from the WFOV. In an attempt to point out measurement differences from the WFOV and NFOV instruments, subtractions between coincident fields were performed. Figure 7a, the difference in emitted flux, shows clearly lower values in the tropics in areas of continental and oceanic ITCZ convection. Areas which show higher IR flux values from the scanner include, the clear ocean regions off the western coasts off continents, and desert regions. Figure 7b, the difference in albedo, shows higher values from the scanner in the same regions where lower scanner IR flux was seen. In the polar regions, the scanner data

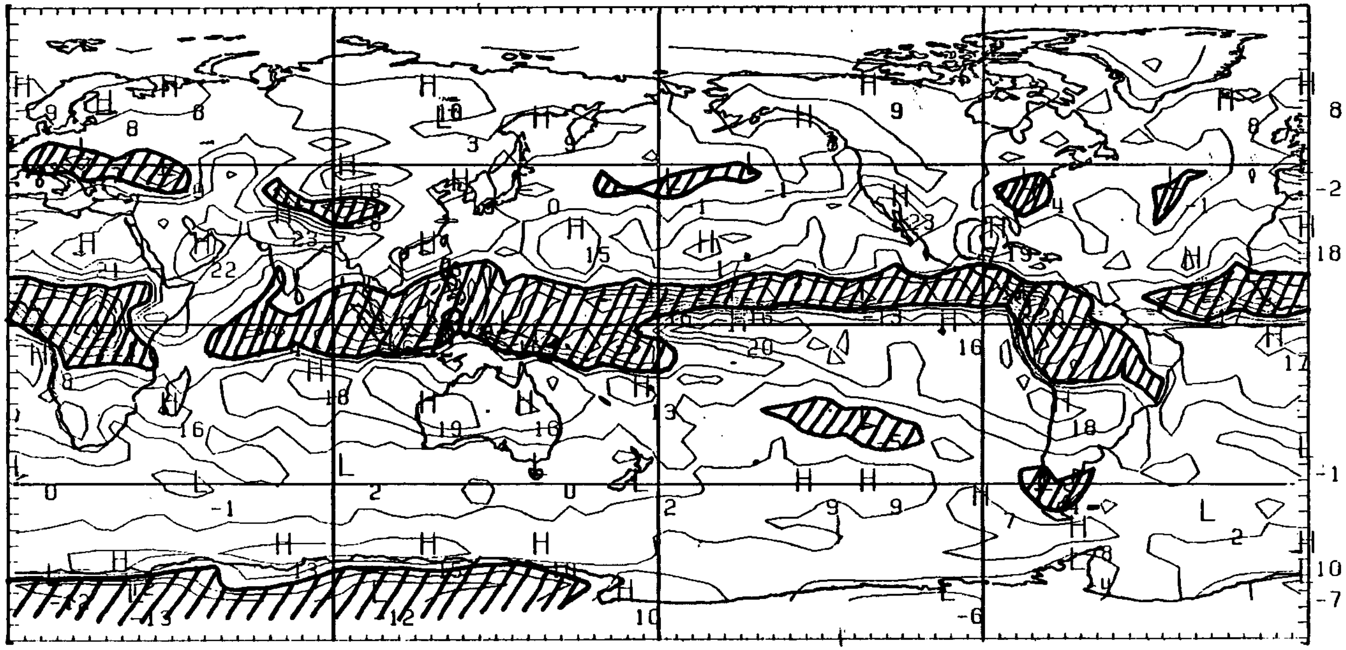

Figure 7a. Emitted flux difference WFOV versus NFOV. Shaded regions are WFOV greater than NFOV.

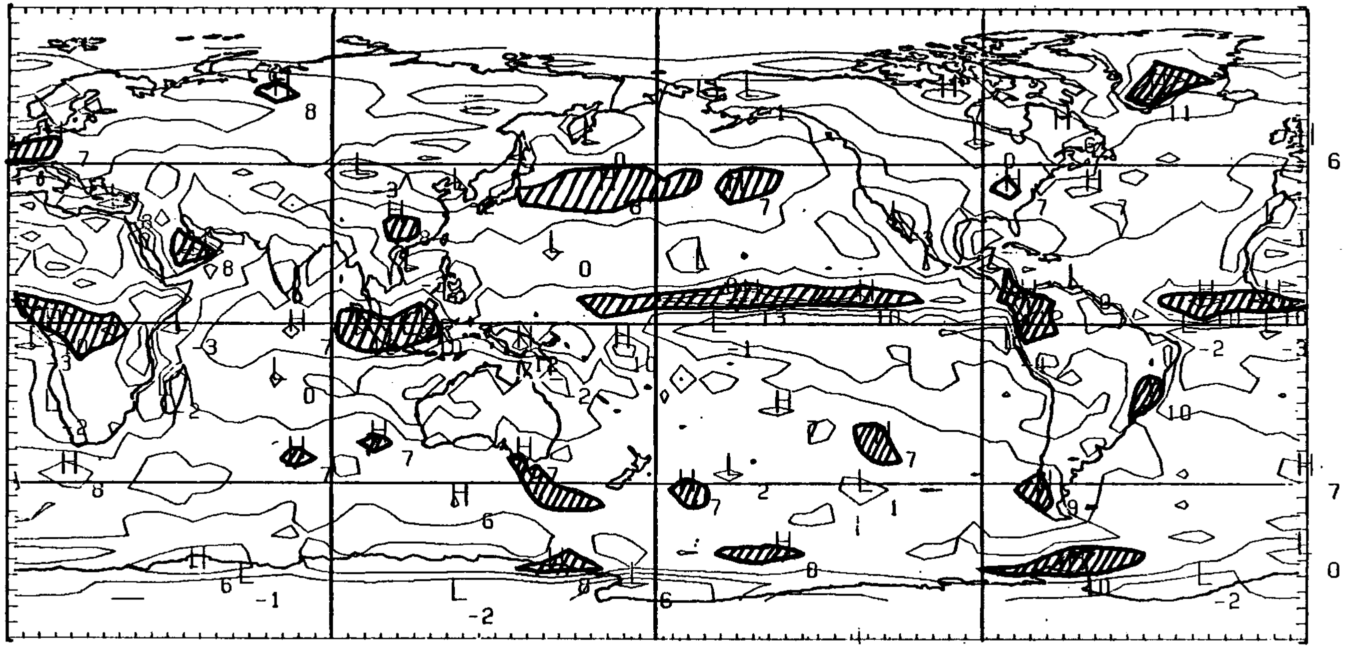

Figure 7b. Albedo difference WFOV versus NFOV. Shaded regions are NFOV greater by more than 6%.

shows Greenland to have a much higher albedo than shown in the WFOV. Also the mid-Northern Pacific shows higher NFOV albedo, believed from synoptic systems that are common to this area. As was shown in Figure 6, the WFOV NET radiation in the tropical oceans is greater then from the scanning data by approximately 10 W/m^2. Using Figure 7, it is easy to deduce which component of the radiation balance accounts for this difference. In the IR flux difference map the WFOV is greater by 10-20 W/m^2, opposite to the effect needed. Consistent with a lower NFOV IR flux, is a higher NFOV albedo of between 5-10%. With an average incident radiation of 415 W/m^2 this amounts to 20-40 W/m^2 lower NFOV NET. Thus it is the large differences in albedo, especially in the areas of tropical convection that accounts for the NET difference between the sensors. This again is an example of the differences in the absolute value of the parameters that could be caused by the different methods of data processing. On the global scale the scanners NET for the year was only a few W/m^2 from balance, while the WFOV instruments showed a much higher residual as a result of it's lower albedo.

The annual day-night difference variation in the IR flux is shown in Figure 8. This was calculated by differencing the day (ascending node), and night (decending node) annual IR flux from the scanner. Areas of greater daytime flux (positive values) include primarily the continental land masses. This is due to daytime heating of the land surface, and cooler radiative temperatures at night. Any daytime cloudiness maximum that could cause higher nightime emission is overshadowed by the daytime heating effect. Over the oceans, the patterns are not as well defined. In the subtropical regions off the west coast of continents (predominately clear regions), higher daytime

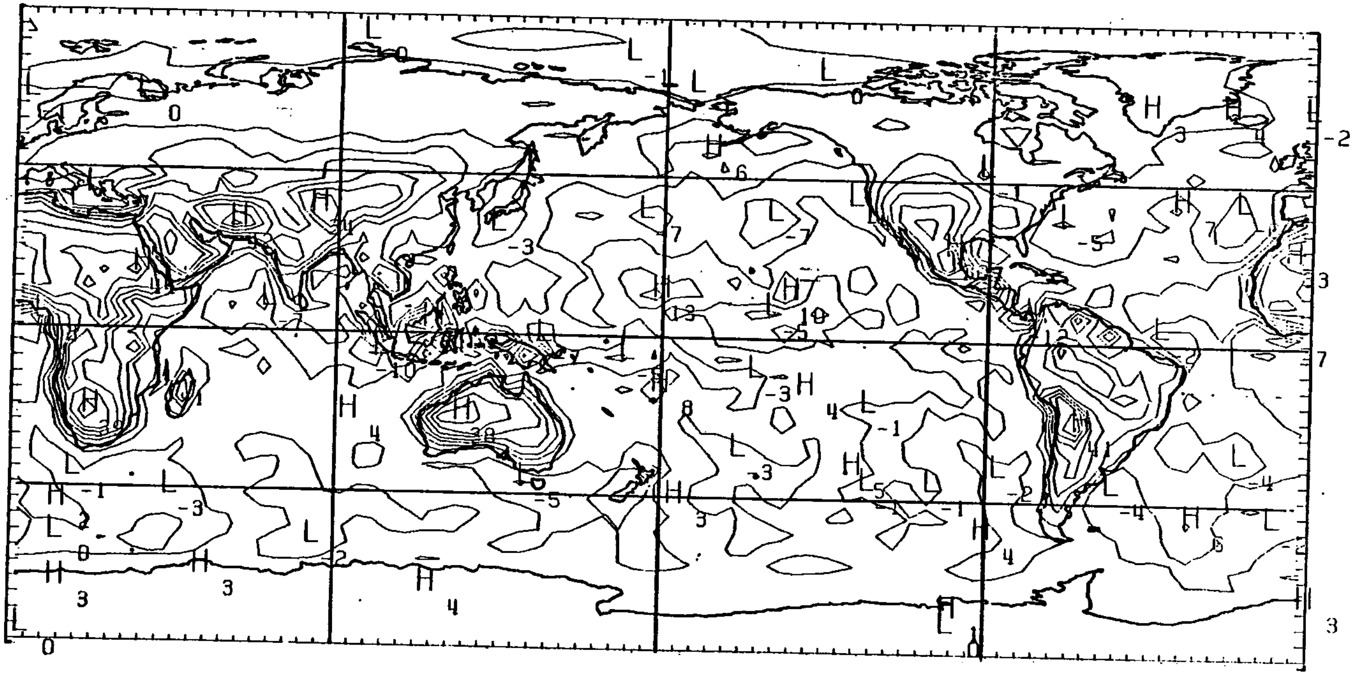

Figure 8. Diurnal difference of emitted flux from scanner November 1978 - December 1979 positive values are daytime maximum.

values are shown. In the midlatitudes oceans a nightime maximum flux suggests a daytime cloudiness maximum and nighttime heat flux from the ocean. In the Pacific ITCZ, higher emission is shown at night, contrary to previous results which showed a tropical nightime cloudiness maximum. A night maximum also occurs off the immediate west coast of Africa, India, and the north coast of South America but for a different reason. The tropical continents have a daytime cumulus convection maximum, thus producing high cirrus clouds that propogate in the tropical easterlies over these oceanic areas. This decreases the daytime emitted radiance of these regions. Off the coast of India, the lower daytime values might be caused by the three months of monsoon cloudiness present over the ocean and an associated daytime cloud maximum.

For the NFOV ERB parameters albedo, NET, and IR flux, global maps of annual range were produced from the monthly averages. Few distinct patterns can be seen in Figure 9, the range of the albedo. The most striking features include the high variation at the north and south latitudes of the polar night terminator, and the high values that follow the Asian ITCZ and the South Pacific Convergence Zone (SPCZ). Here annual variation of 30-40% in the albedo results from the movement of these zones throughout the year. Figure 10, the IR flux yearly range, also shows high variability in these areas. High values are also seen on the continents due to the large component of incident radiation in the summer months and warmer continental temperatures. In the NET range map, Figure 11, major differences between the two hemispheres can be seen. The tropical area 10°N - 10°S, shows little yearly variation due to the small variation in the annual incident radiation. Indeed the range, and the yearly cycle of NET radiation are found to be almost

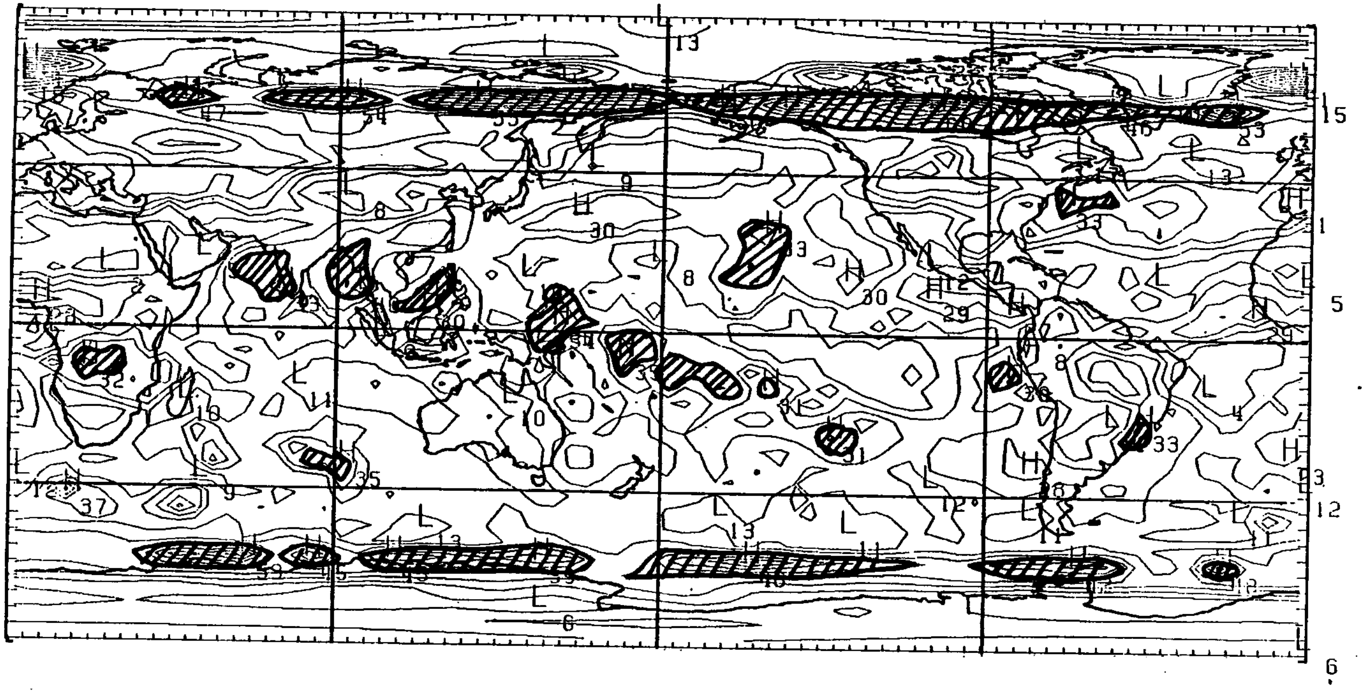

Figure 9. Annual range of NFOV albedo November 1978 - October 1979. Shaded regions show variation of greater than 25%.

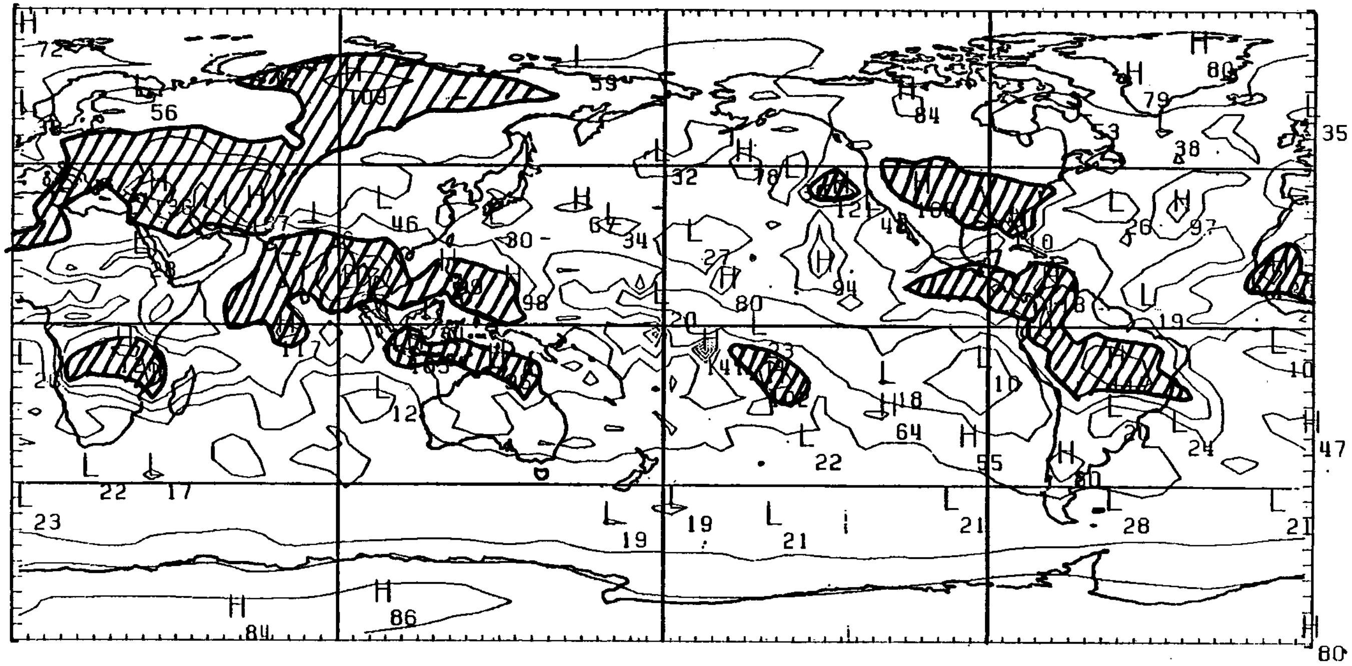

Figure 10. Annual range of NFOV emitted flux. Shaded regions show variation of greater than 80 W/m^2.

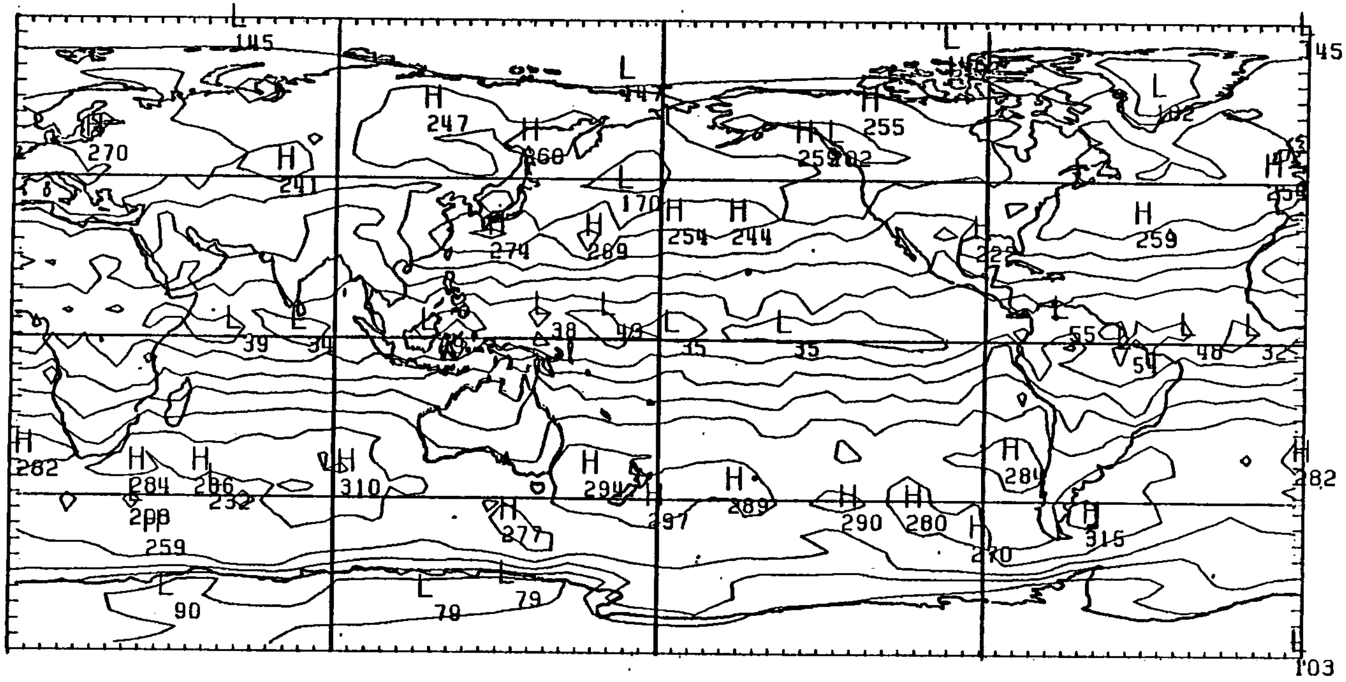

Figure 11. Annual Range of Net Radiation

totally dependent on the seasonal incident radiation changes, thus the NET range increases with increasing latitude in both hemispheres. The oceanic areas show the highest annual NET range because over the continents the summer cumulus convection reflects a portion of the increased incident. This effect is the cause for the Southern Hemisphere to show much higher values due to a smaller percentage of land area then the Northern Hemisphere. The polar regions vary little compared with their variation in incident radiation. This is due to their high albedo surface which reflects the major part of the incoming radiation.

Global annual averages were computed for each ERB parameter by combining the monthly averages from each of the 12 months. Each monthly value as well as the annual average for the major parameters are given in Table 5. Of special note is the 3% difference in albedo between the WFOV and NFOV instruments. This would account for the difference seen in the NET radiation between the sensors, as a 3% difference would amount to 10–15 W/m^2 change. The 3.5 W/m^2 deficit for the annual NFOV NET is well within the instrument accuracy. It has been suggested that the 3% albedo difference in the sensors has come about primarily through bias in the scanning radiometer data processing (Vemury, 1983). As this might be confirmed by future error analysis at NASA-Goddard, the 3% difference should not be assumed absolute. Table 6 compares some calculated values from N7 with that of previous work.

Table 5

Monthly and Global Earth Radiation Budget Averages

		N	D	J	F	M	A	M	J	J	A	S	O	Ave.
Albedo	N. Hemis.	312	302	302	311	314	320	322	316	308	295	286	289	306
WFOV (%X10)	S. Hemis.	324	321	313	303	295	284	277	266	270	275	290	310	294
.2-4μm	Global	320	315	310	306	304	305	307	301	296	287	288	301	303
NET	N. Hemis.	-61.6	-68.1	-58.0	-29.4	8.2	44.5	65.5	74.6	68.3	50.3	20.3	-18.6	8.0
Radiation	S. Hemis.	83.9	99.	95.1	67.8	26.3	-22.3	-58.1	-73.8	-68.	-38.7	4.5	47.3	13.6
WFOV W/m^2	Global	11.2	15.4	18.5	19.2	17.2	11.1	3.7	.4	.1	5.8	12.4	14.3	10.8
IR Flux	N. Hemis.	224	224	225	229	228	232	236	239	243	242	239	233	233
NFOV W/m^2	S. Hemis.	236	234	236	232	232	231	230	232	231	231	230	232	232
AN+DN	Global	230	229	231	231	230	232	233	236	237	237	235	233	233
Albedo	N. Hemis.	339	327	317	330	334	350	348	348	349	327	315	321	334
NFOV	S. Hemis.	342	343	333	339	325	304	311	305	314	306	318	332	323
(%X10)	Global	341	338	328	335	329	331	335	335	338	319	316	327	331
NET	N. Hemis.	-72.8	-79.3	-75.3	-44.3	-1.1	36.0	55.0	62.5	51.2	36.0	5.4	-34.2	-5.1
Radiation	S. Hemis.	75.6	87.6	84.9	52.4	9.4	-45.8	-76.	-91.2	-85.3	-54.4	-12.	32.5	-1.9
NFOV W/m^2	Global	1.4	4.1	4.8	4.1	4.1	-4.9	-10.5	-14.4	-17.1	-9.2	-3.3	-.8	-3.5
IR Flux	N. Hemis.	220	218	217	218	221	225	230	235	239	237	233	226	227
WFOV W/m^2	S. Hemis.	230	228	229	227	226	223	222	224	223	224	223	225	225
AN+DN	Global	225	223	223	223	223	224	226	229	231	231	228	225	226

Table 6
Comparison of N7 ERB with previous results

	Northern Hemisphere			Southern Hemisphere			Global		
	ALB (%)	IRF (W/m^2)	NET (W/m^2)	ALB (%)	IRF (W/m^2)	NET (W/m^2)	ALB (%)	IRF (W/m^2)	NET (W/m^2)
Nimbus 7 Scanning Radiometer	33.4	233	-5.1	32.3	232	-1.9	33.1	233	-3.5
Raschke et al. Nimbus 3 (1973)	28.7	241	-1.4	28.0	240	7.0	28.4	241	2.8
Stephans, Campbell, Vonder Haar (1981)	31.0	233	5.1	29.7	235	7.2	30.2	234	6.2

3.1.2 Monthly

When comparing the yearly albedo cycle from the scanner and non-scanner, the 3% difference for the annual mean certainly does not account for all the variations seen. Figure 12 contains plots of data from the NFOV and WFOV instruments for the global, Northern Hemisphere and Southern Hemisphere albedo. It might be expected that the yearly cycle would be rather uniform due to the importance of the seasonal changes, but examination of the NFOV global plots shows the annual cycle is not well defined. For the Northern Hemisphere minimums are found in January and September, with maximums in April and July. For the WFOV a more seasonal cycle is evident in the global plot, with the exception of April and May where the values seem higher then expected. The reason for this anomaly is not apparent in either of the hemispheric plots, but is caused by a combination of changes in snow-ice cover and illumination of the high albedo polar regions (Vonder Haar, 1981). The large

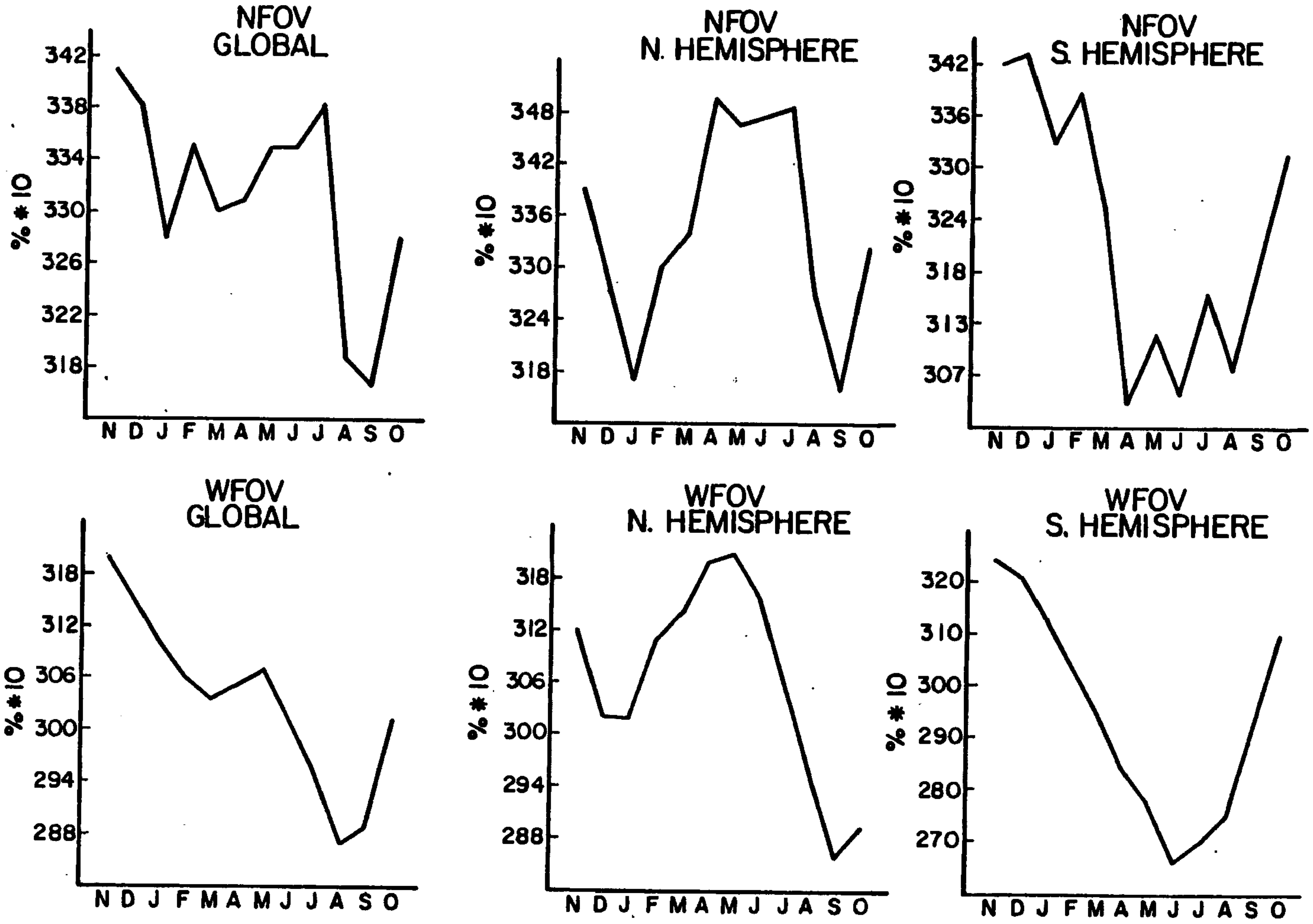

Figure 12. NFOV and WFOV albedo annual cycles.

differences in the global annual cycle of albedo between the WFOV and NFOV should be of some concern. The NFOV has much larger relative values from May through July that could be caused by the following problems. First the northern hemisphere (NH) albedo shows this same larger relative values. During the months of May and June solar radiation is becomming incident at a much higher zenith angle on the NH high altitude zones. Errors in the NFOV albedo data processing that may occur at high viewing angles similar to what may have caused the 3% difference in global albedo, may also be causing this difference. Second, the southern hemisphere NFOV July albedo increases while the WFOV decreases. During this month, one more zone was added to the SH average. This zone was at a high latitude, having a high albedo, and wans't included in the WFOV data. Third, the difference in the albedo from the two sensors for these months amount to only around 2%. This albedo difference is less then the average difference and could be induced anywhere in the NFOV or WFOV data processing. There are probably many other possible sources for error not discovered yet, and these results should be used with this in mind.

Figure 13 shows the cycles of average monthly IR flux. Here the annual cycles are much better defined, especially in the global and Northern Hemisphere plots. A plot of the data after removal of the first harmonic is also presented, and evidence of a second harmonic can be seen. This is believed a result of the two period cycle of incident radiation in the tropics. As might be expected a second harmonic is also seen in the NET radiation plot, Figure 14, but the annual cycle of incident radiation is clearly the major contributor. By examining the hemispheric graphs with the first harmonic removed it is easily seen

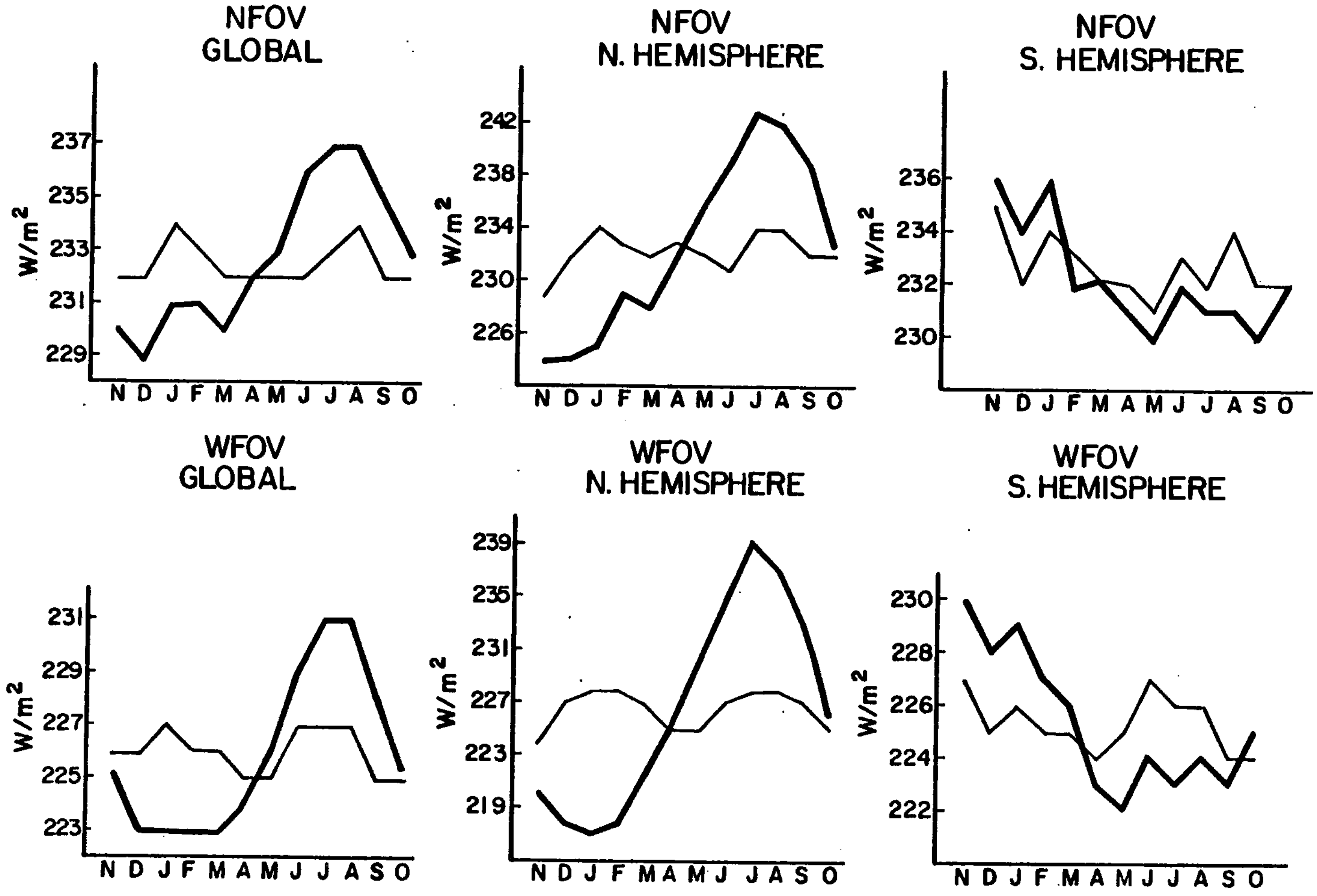

NFOV GLOBAL

NFOV N. HEMISPHERE

NFOV S. HEMISPHERE

WFOV GLOBAL

WFOV N. HEMISPHERE

WFOV S. HEMISPHERE

Figure 13. WFOV and NFOV emitted flux annual cycles. Thin line is cycle with first hormonic removed.

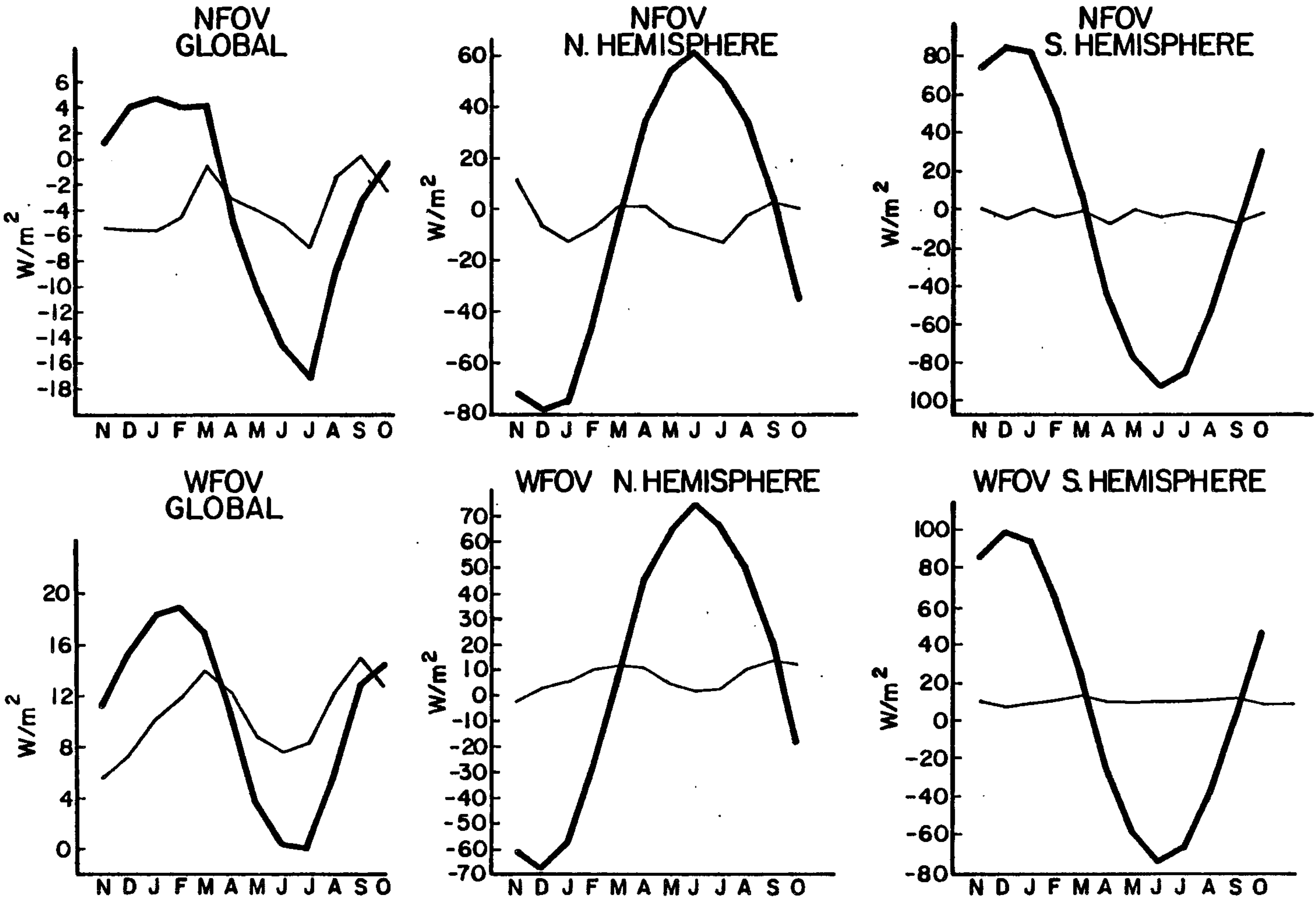

Figure 14. WFOV and NFOV NET radiation annual cycles. Thin line is cycle with first hormonic removed.

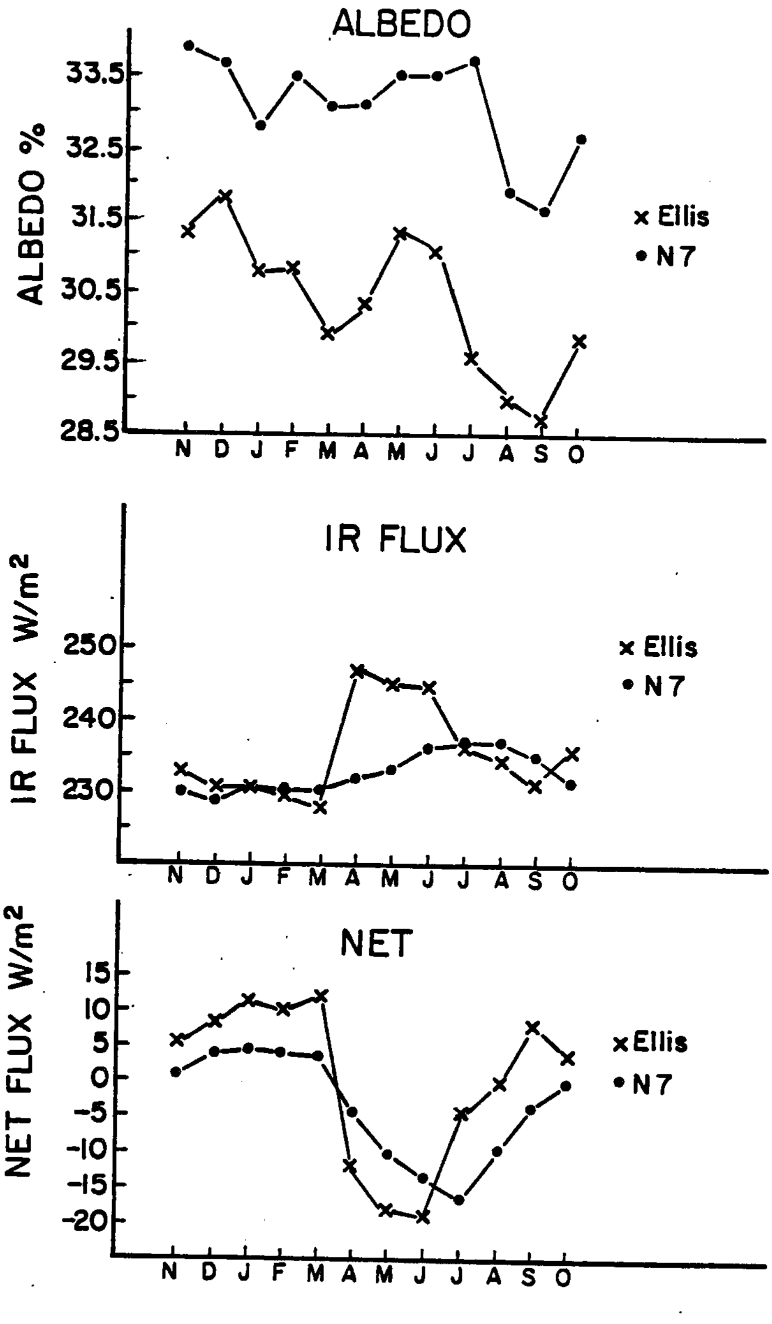

Figure 15. Nimbus 7 scanning radiometer cycles compared with Ellis, et al. (1978).

that all of the global variation outside of the seasonal cycle is caused by variations in the Nothern Hemisphere. This is due to the continental effects that are not present in the Southern Hemisphere and to movements of the ITCZ in the Northern Hemisphere. Vonder Haar and Ellis (1977) showed that over half the amplitude of the annual NET cycle is induced through changes in Earth-sun distance.

A comparison of data cycles from Ellis et al. (1978) and that from the N7 scanner is shown in Figure 15. The N7 plot of IR flux does not show as wide a yearly variation as those from Ellis. The graph of albedo shows higher relative values in May through July from the NFOV scanner. The Ellis cycles, which are a combination of over 29 months of ERB data, show nearly the same annual pattern as does the WFOV. This would tend to substantiate the WFOV albedo cycle rather than the NFOV. The cycles of net radiation show this albedo effect with lower N7 NET values after April.

3.2 Zonal Radiation Budget

3.2.1 Annual

This section will present results from zonal averaged (ZA) quantities, the next step in the progression toward higher spacial scales. Zonal averages of the range maps (Figures 9-11) were computed and latitudinal plots of these values are shown in Figures 16-18. The data values are a measure of the annual variability of the specific latitude zone. Figure 16 shows that the scanning radiometers sense higher albedo zonal variation at the Northern Hemisphere (NH) seasonal polar night terminator, at the subtropical boundary of synoptic systems (32°), and between 0°-10° N in the zones which the ITCZ changes

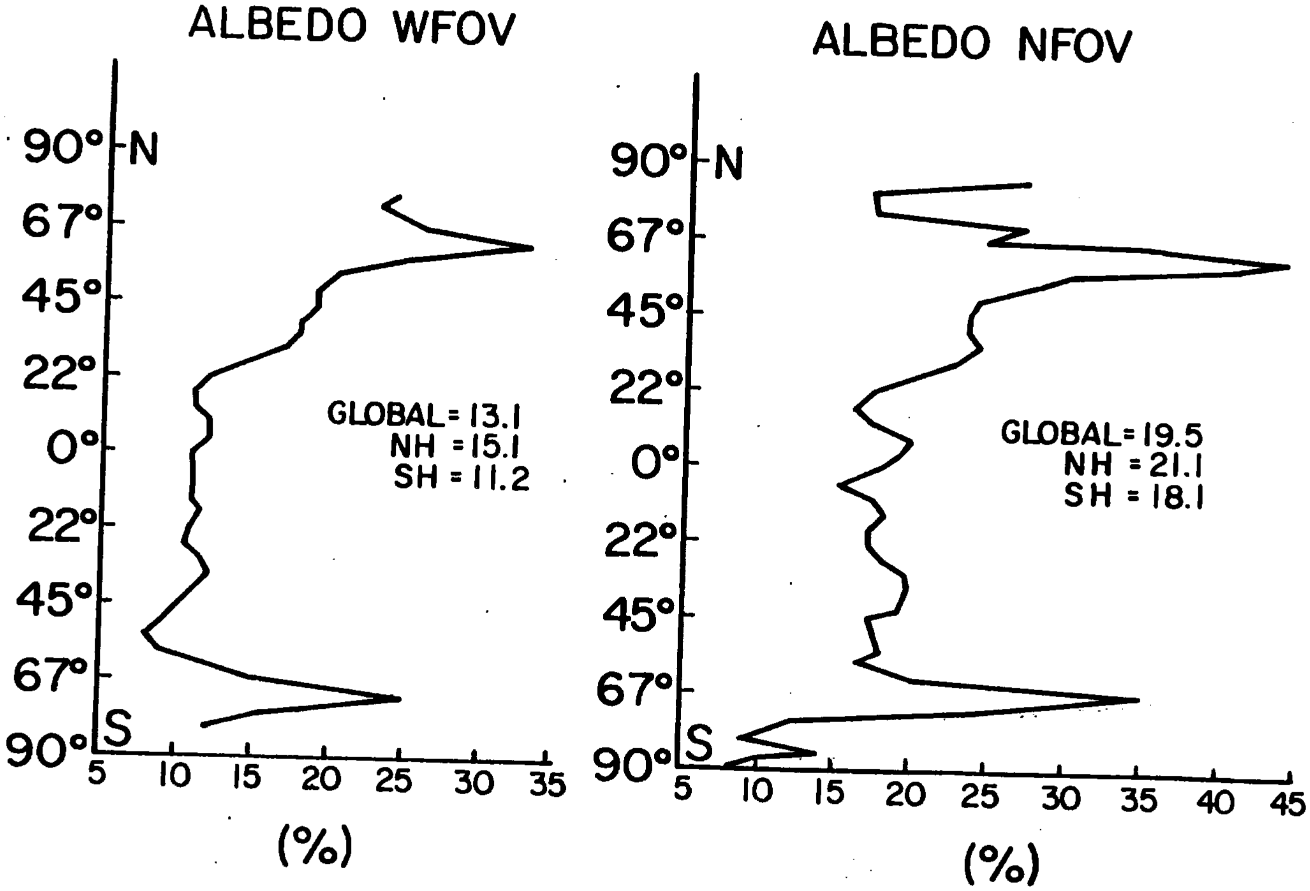

Figure 16. Zonal average annual range of albedo.

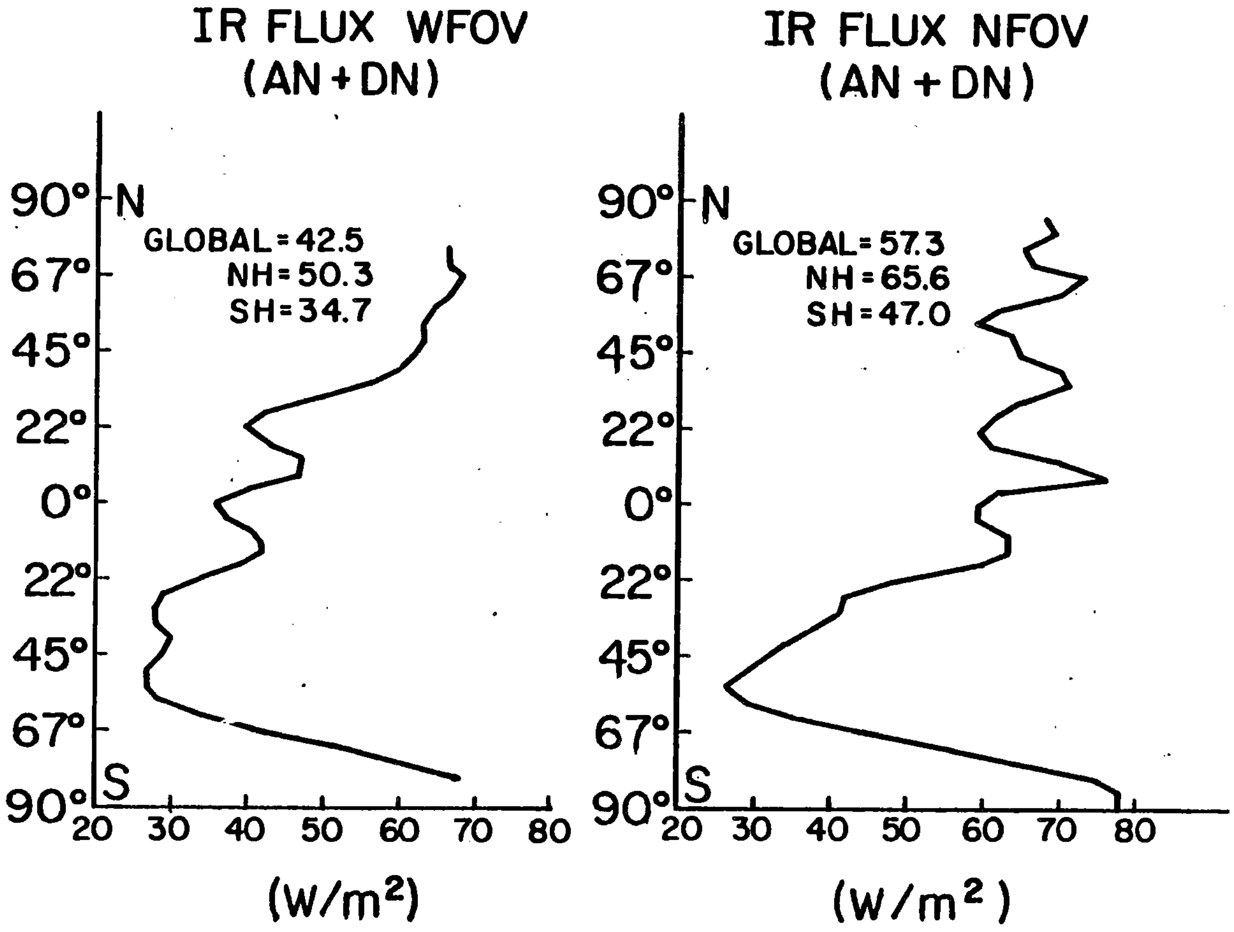

Figure 17. Zonal averaged annual range of emitted flux. Ascending plus descending nodes.

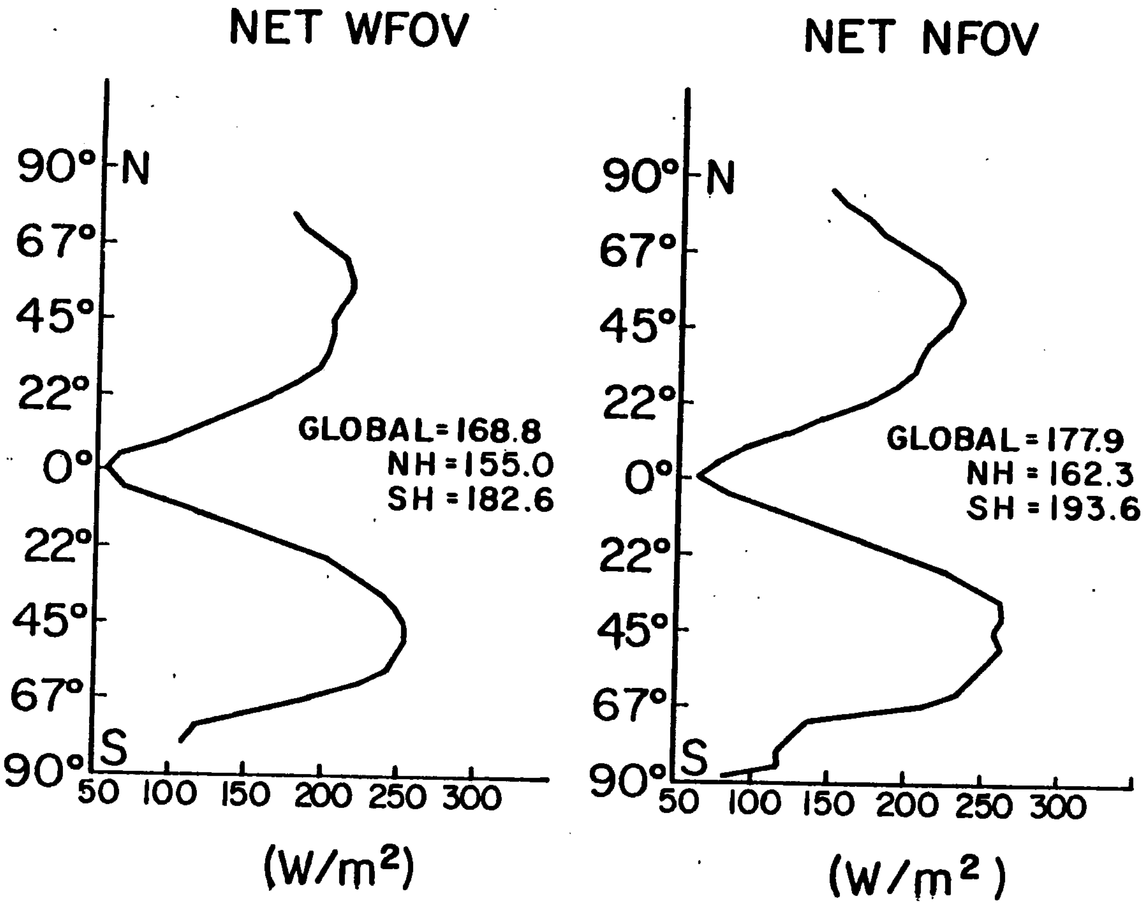

Figure 18. Zonal averaged range of NET radiation.

location. Zones of smaller variation include the dry subtropical areas which consist primarily of continental deserts in the NH, and oceanic areas in the Southern Hemisphere (SH). These features are easily recognizable in the NFOV data, but are not as apparent in that from the lower resolution WFOV instrument. In Figure 17, the ZA range of IR flux, an obvious hemispheric difference shows the SH zones to have much less variation than the NH. In the SH there is a greater percentage of ocean area which acts to absorb excess radiation and keep the surface temperature and IR flux variation low. Compared to the NFOV, the WFOV graph shows lower variability in the polar regions and near the boundary of the ITCZ. The NFOV graph shows higher latitudinal variation in the NH with an alternating pattern of high and low variation. Causes of this pattern, their location, and the relative variation are: equatorial constant cloudiness (0° low), changing ITCZ (9° high), subtropical deserts (22° low), continental heating (36° high), and finally the seasonal ice-line (68° high). The ZA range of NET radiation, Figure 18, clearly shows the effect of the changing incident radiation in the mid-latitudes and the low variability of the tropics. The polar regions, especialy the south pole, show much lower values than the mid-latitudes. this is because the NET radiation for these regions is not calculated for the winter months that have zero incident radiation. In the summer months, the incident increases is maximum but still isn't as large, due to high zenith angle as the incident in the mid-latitudes. Of the summer incident that is available, the majority is reflected by the high albedo snow and ice surface.

In order to find areas within a zone that differ from the zonal average, Figures 19 and 20 were created. These maps, labelled

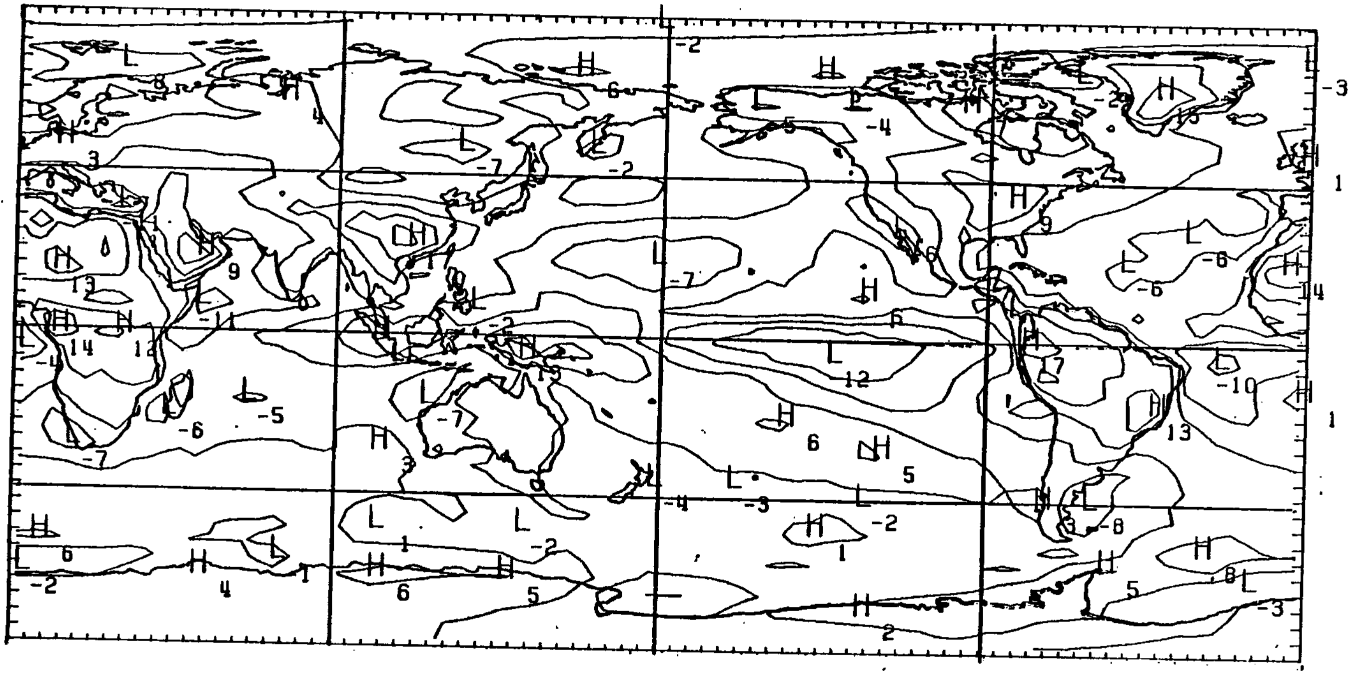

Figure 19. Albedo NFOV difference from the Zonal Mean November 1978- October 1979 (W/m^2)

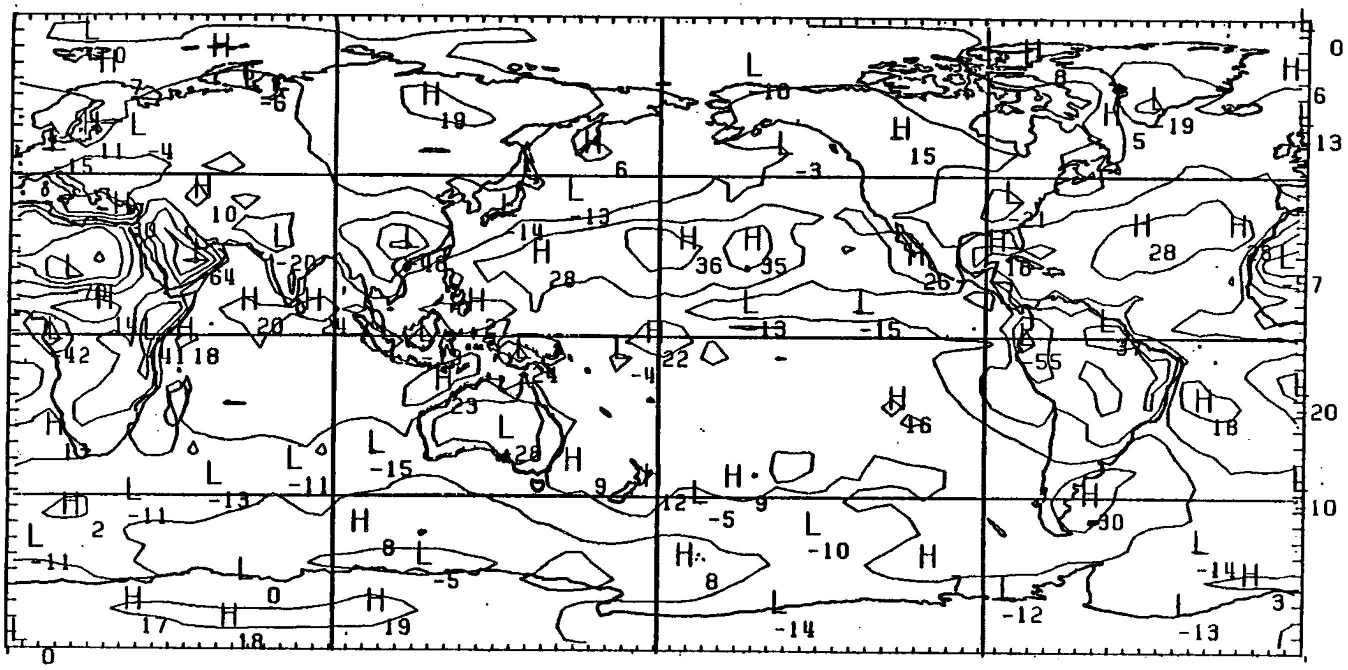

Figure 20. Net Radiation NFOV Difference from the Zonal Mean. (W/m^2)

Difference from the Zonal Mean (DZM), show how each point differs from the zonal average. Figure 19 shows what extreme albedo variability is present within each latitude zone, with the continents having higher values while the ocean surfaces show lower. There are exceptions where oceanic areas are higher than their ZA: the island continent of Indonesia, the South Pacific Convergence Zone, and the Pacific ITCZ west of South America. Figure 20, the DZM of the NFOV NET radiation again shows the large land-ocean gradients and the lower values over the cooler oceans. Note the extremely low values over Saudi Arabia and the Sahara which show how anomalous these areas are in the NET radiation budget. These figures show how highly variable individual areas are within the ZA, and what large meridianal gradients are present. Vonder Haar (1972) produced the DZM map of the NET radiation for 17 seasons, defining many of the same areas as in Figure 20 but with much poorer resolution. The N7 scanner data shows these areas to be much larger and have greater deviation values.

The latitudinal distribution of the NET radiative balance, albedo, and emitted longwave radiation are shown in the zonal radiation budget graphs, Figures 21-22. Annual profiles from both the NFOV and WFOV show some hemispheric symmetry, with the exceptions being the two polar regions and the displaced local minimums of IR flux and NET radiation at 10°N. Scanning radiometer measurements at 10° show differences in the albedo of 8-10%, IR flux of -35 W/m^2, and NET of -20 W/m^2 from subtropical values. These anomalies are due to average ITCZ cloudiness which has an averaged position of 5°N. The high emission and lower albedo zones at 25 latitude are evidence of the subtropical dry zones in the downward branch of the Hadley cell. Gradients between subtropical

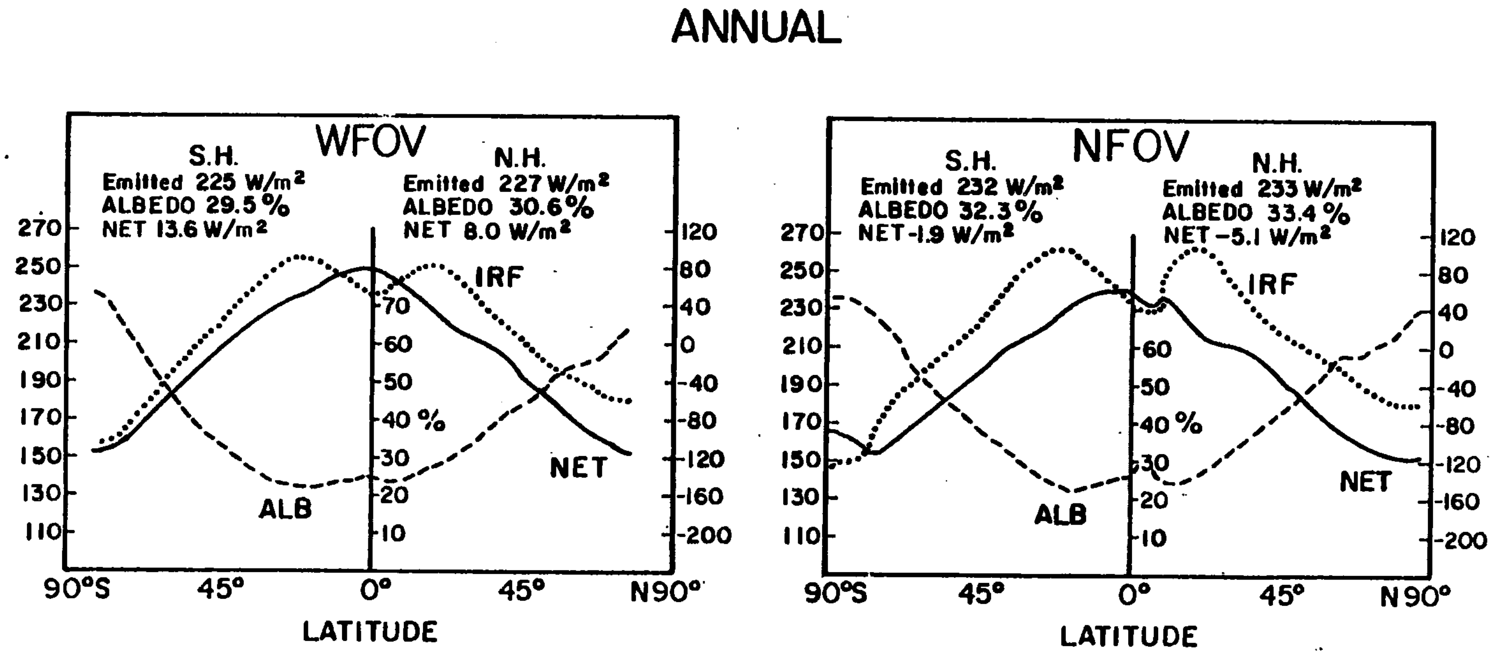

Figure 21. Annual zonal averaged WFOV and NFOV albedo, emitted flux, NET radiation.

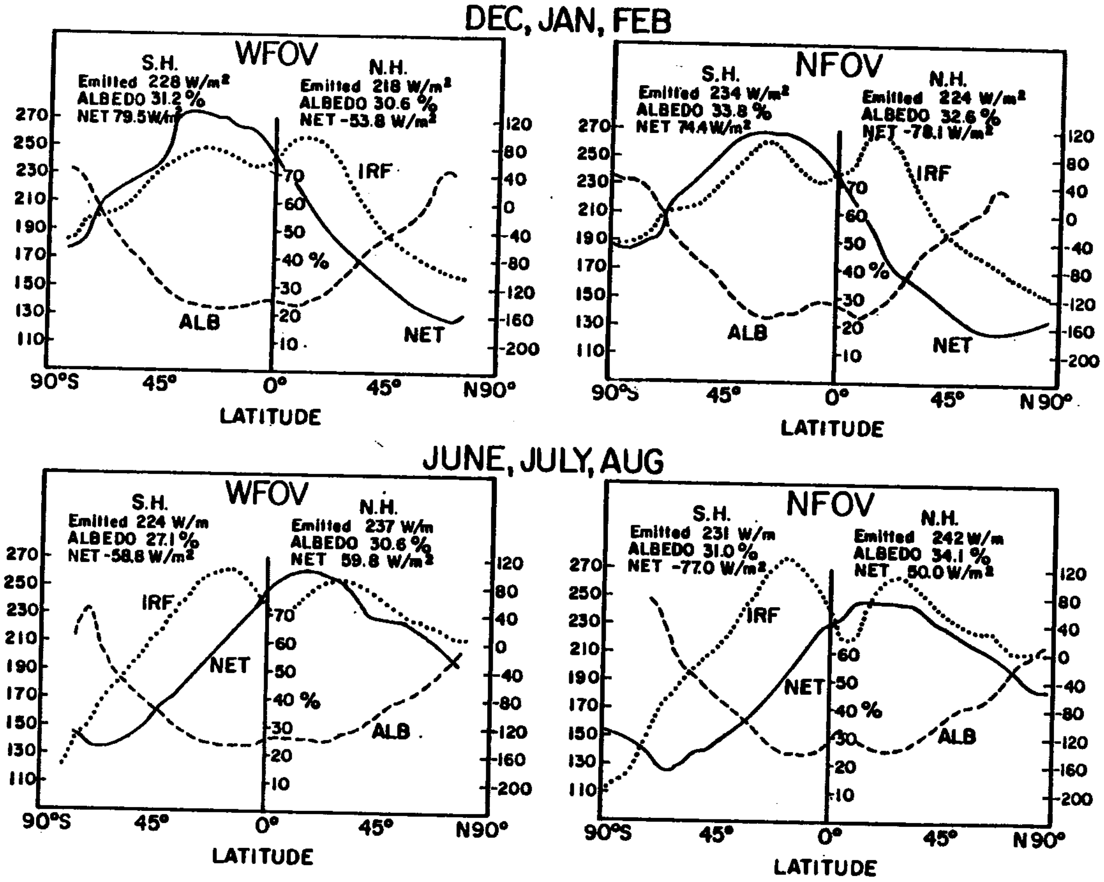

Figure 22. Seasonal zonal averaged WFOV, NFOV albedo, emitted flux, NET radiation.

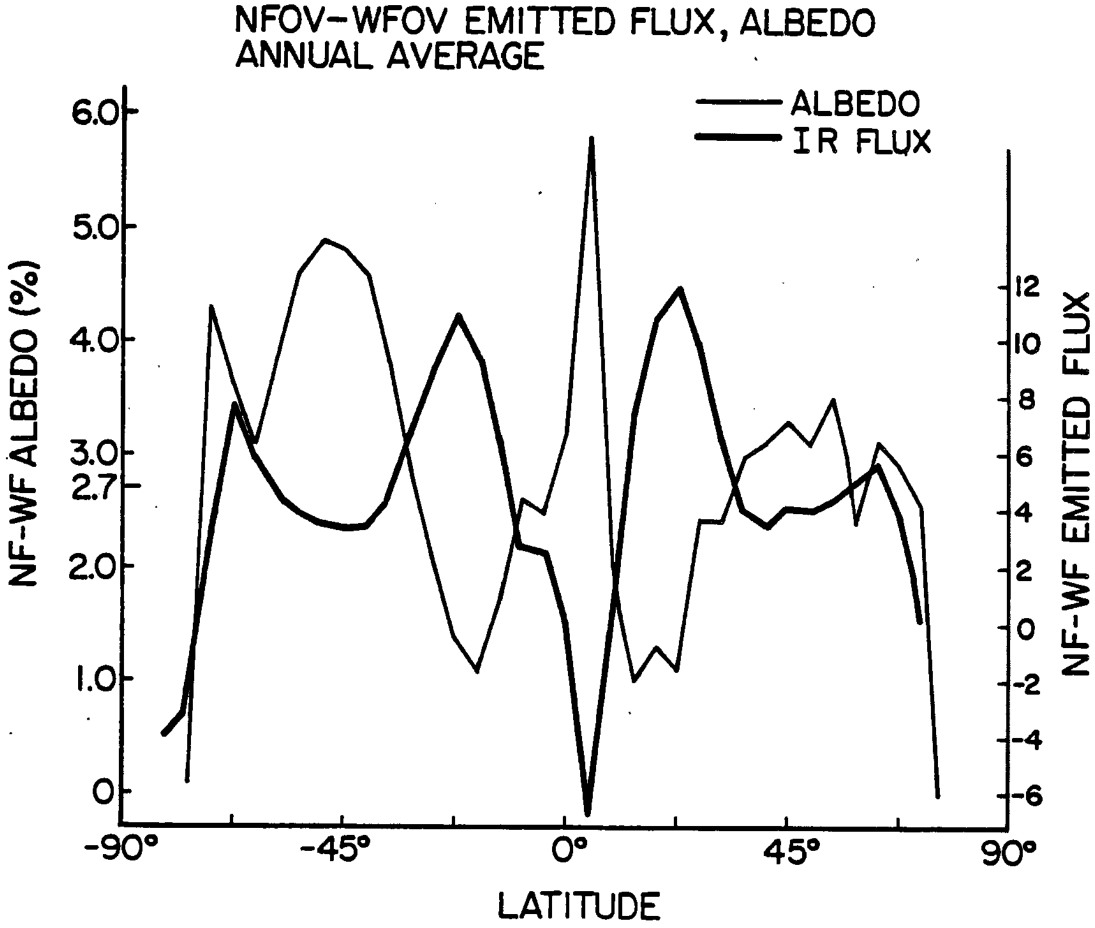

Figure 23. NFOV versus WFOV difference of zonal averaged albedo and emitted flux.

areas and the ITCZ are much greater from the scanning radiometers than in the WFOV data or previous WFOV results. Figure 22, the prime seasonal results, shows that the location of the ITCZ follows the maximum incident radiation, shifting into the summer hemisphere. The seasonal maximums of NET radiation are shown dependent on this same cycle. In December, January, and February the SH has a net gain of near 80 W/m^2 while the NH average loss is over 50 W/m^2.

A graphical representation of the scanner versus non-scanner data, Figure 23, is proof of the scanners advantage in sensing important high resolution features of the general circulation. The difference of the NFOV and WFOV albedo and IR flux zonal averages are plotted after shifting the ordinate scales in order to zero the average difference of the values. The scanner senses higher albedo in the location of the ITCZ cumulus convection, mid-latitude synoptic clouds, and at the latitude of the seasonal ice-line with lower albedo shown in the subtropics and over polar regions. The IR flux difference is almost the reciprocal of the albedo, showing higher emitted flux in the subtropics and lower in areas of cloudiness. Radiation budget gradients from the scanner radiometers between the subtropics and the ITCZ are 20 W/m^2 greater for IR flux and over 5% larger for albedo. Higher gradients in these areas must be taken into account when modeling atmospheric energetics and validating global climate models.

3.2.2 Monthly

Time series of the zonal averaged NFOV ERB parameters, created from the monthly data are presented in Figure 24-26. In December, January and February when the ITCZ is positioned in the SH, there is a broad

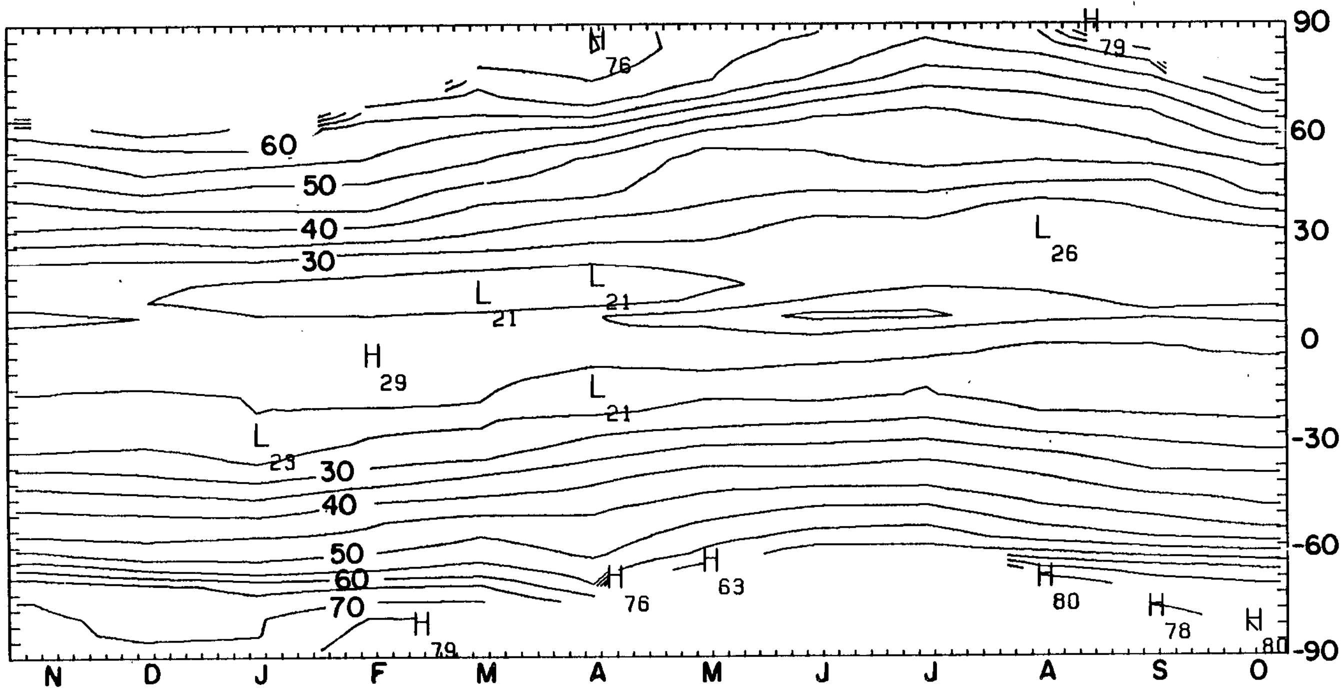

Figure 24. Zonal average albedo time series November 1978 - October 1979.

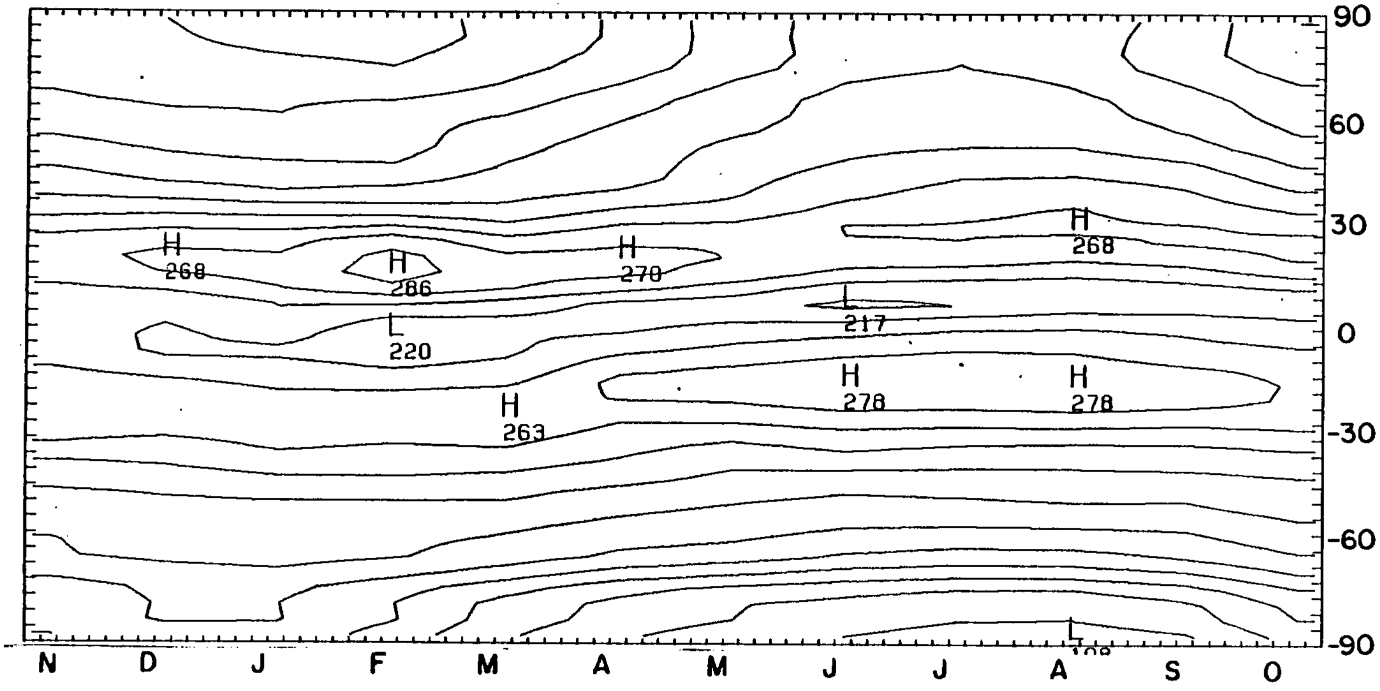

Figure 25. Zonal average emitted flux time series. (W/m^2)

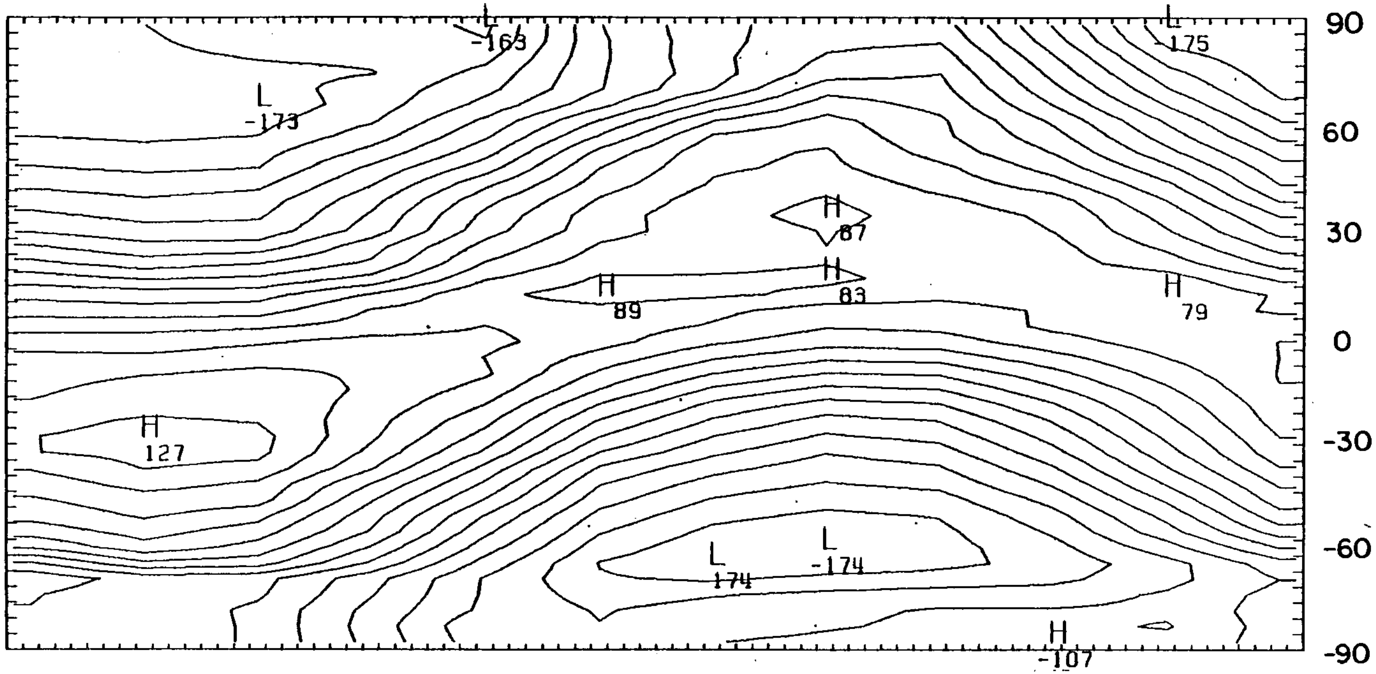

Figure 26. Zonal average NET radiation time series.

area of increased equatorial albedo suggesting an ITCZ that is not as intense. In June, July and August, smaller latitudinal extent of the ITCZ is seen due to a stronger, more active NH ITCZ. Figure 25, the IR flux time series, clearly shows the seasonal movement of the ITCZ bordered by the clear sky, higher emitting subtropical zones. The asymmetry between hemispheres is shown in Figure 26, where a much higher NET radiation is found in the Southern Hemisphere's summer than in the NH. Increased cloud cover over the NH summer continents may cause reflection of energy that in the SH is included as higher NET.

3.2.3 Daily

The N7 scanning radiometer allows us to examine high resolution, daily broadband earth radiation budget data for the first time. One of the most interesting day-to-day changes occurs when the winter NH wave amplitude increases resulting in a blocking situation. There were several of these events during the winter of 1979, the most persistent of which occurred during the week of March 20-27. During this time the 500 mb pattern showed highly non-zonal flow resulting in steep ridges and deep troughs around the globe. One week earlier on March 13, we were in a regime of low wave number and highly zonaly flow. Figures 28-30 present the NH zonal radiation budgets for March 13th (zonal case), and for March 21st (blocking case). Figure 27, the zonal IR flux, shows the effect of the blocking situation on the emitted flux. In the mid-latitudes there is lower existance between 27° and 41° and higher between 41° and 68°. This is due to the increased transport of colder air south and warmer air north, decreasing the gradient throughout the mid-latitudes. Figure 28 shows the blocking case albedo

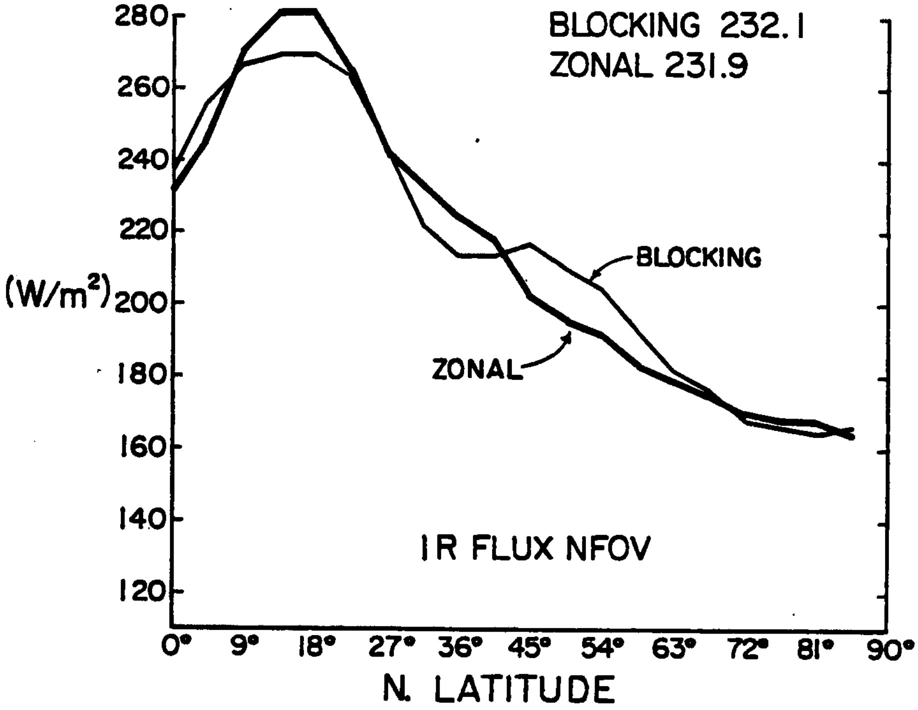

Figure 27. Northern Hemisphere zonal average NFOV emitted flux for blocking flow and zonal flow cases.

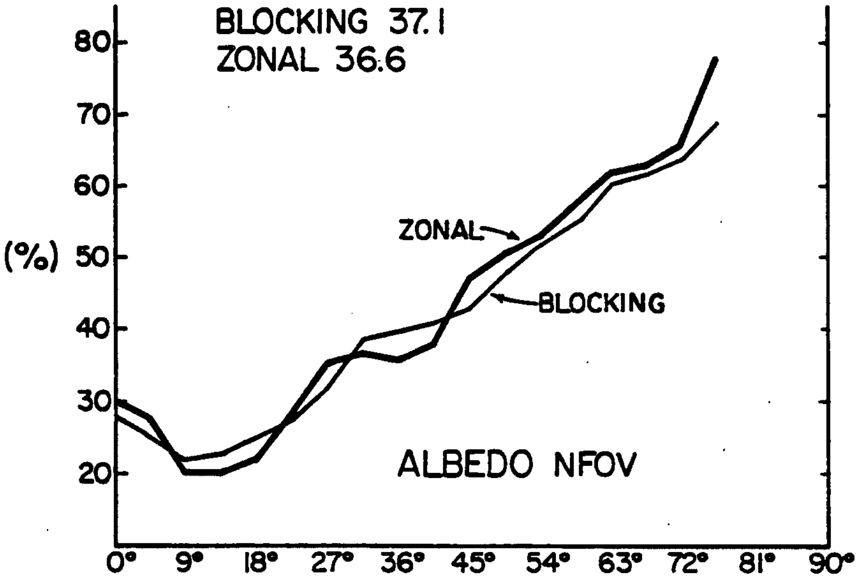

Figure 28. Same as for Figure 27 except for albedo.

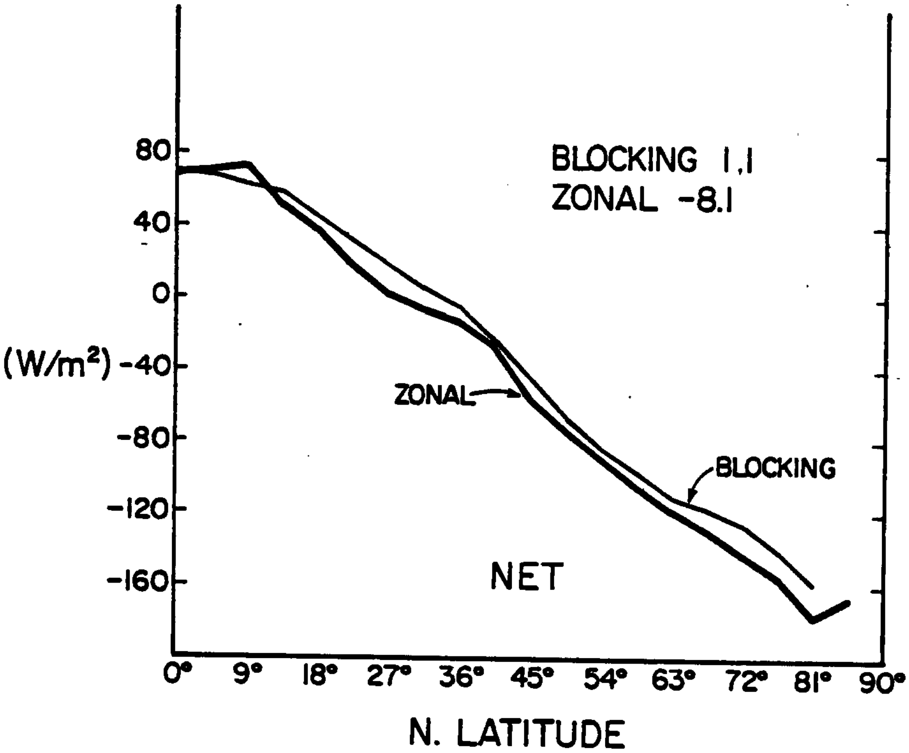

Figure 29. Same as Figure 27 except for NET radiation.

to increase between 31° and 41°, and decrease above 41°. This change in albedo is another factor involved in the changes of IR flux. The greatest fluxuation in emitted radiation occurs between 45° and 55°, where more than a 15 W/m^2 change is seen. Over these same zones the albedo correspondingly changes 3-4%. The most interesting effect of the mid-latitude blocking occurs in the tropics and subtropics. Here the emitted gradient decreases by 34% (18 W/m^2) and the albedo gradient by 40% (4%). This suggests that intensity changes in the Hadley circulation could be caused by, or be the cause of mid-latitude changes in wave amplitude. The zonal average of NET radiation, Figure 29, is remarkably constant, showing only minor variation at 9° and 40°. The average difference of 9 W/m^2 is typical of the change expected in the annual cycle for one week. Future studies will discover what effect the localized radiation budget has in the initiation and break down of these blocking situations. It seems apparant that if the case studied is typical, the blocking patterns exert no major impact on the general zonal gradient of energy exchange between earth and space.

3.3 Regional and Local ERB Studies

3.3.1 Monthly

The Nimbus 7 scanning radiometer measures broadband radiation at 150 km resolution (mapped into 500 km areas), thus allowing regional and synoptic scale ERB studies. Climatologists have often examined small regional areas that show large ERB variability for the first signs of climate change. These include the seasonal polar ice-line, and tropical areas that have important energy transports. In this section the annual cycles of areas with high seasonal NFOV ERB variation will be presented.

Areas for study were choosen from Figure 9-11, the annual NFOV range maps. The annual ERB cycle for 20 areas were examined, but it was decided that only six areas were needed as a representative sample of the different causes of high ERB variation. These regions, their latitude-longitude boundaries, and their ERB parameter annual range are listed in Table 7.

Table 7
Selected Regions of Abnormal Annual ERB Variability

		ALB	IRF	NET	INCIDENT
Tibet Plateau	31.5°-40.5°N 80°-105°E	9.6%	55W/m^2	131W/m^2	290W/m^2
Sahara Desert	18°-31.5°N 10°W-31.5°E	6.0	47	106	183
Equatorial Atlantic	13.5°N-4.5°S 40.5°-13.5°W	7.1	20	34	44
Pacific Ocean off West Coast of South America	9°-22°S 105°-85°W	16.1	10	182	170
South Pacific from Australia-New Zealand	36°-49.5°S 156°E-168°W	17.5	22	274	384
Bay of Bengal	9°-18°N 90°-99°E	34.3	120	91	103

Comparisons with the WFOV data are presented for two of the areas where specific differences in the measurements are seen as important to understanding the ERB changes. The six areas vary in size, and usually the larger the area, the closer the WFOV compares to the NFOV. Although most of the areas show regular annual cycles, some have distinct variations that make them unique. In one case the first harmonic (annual of other cycle) was removed from the data in order to point out these variations.

Figure 30-35 show the annual cycles for each area plotted over consistent ordinate values so that the relative change between areas can be noted. The continents show very little change in the NET radiation because they have high emittance during periods of high incident radiation. The oceanic areas with their large change in cloudiness usually show the greatest variation in the ERB outside of the continental ice-line albedo changes, and thus four out of the six regions are oceanic. The two land areas are unique only due to their relative stability in one or more of the ERB components.

The ERB of the first continental area, the Tibet Plateau, is presented in Figure 30. This region is high in elevation, cutoff from moisture sources, consisting primarily of barren ground or snow cover. It is characterized by low variation in the albedo (less than 10%), due to snow cover in winter and cumulus activity in summer. This area also shows low variation of IR flux (55 W/m^2). Combine this with a high annual change in Incident (290 W/m^2), and the NET variability is then over 130 W/m^2. The other continent areas at this latitude show much greater variation of albedo due to winter snow versus spring and summer growth. Asian continental areas show albedo changes of over 15% and the Western U.S. of near 25%.

The other anomalous land area is the Sahara desert, Figure 31. With little change in the annual cloud cover, the albedo variation of 6% is the lowest of all the areas presented. The IR flux variation reflects the constant annual temperature and is also very low at 47 W/m^2. The non-scanning WFOV data is also included to point out an interesting difference in the emitted flux cycles. In March, equatorial cloudiness impinged on the southern part of the region. The scanning

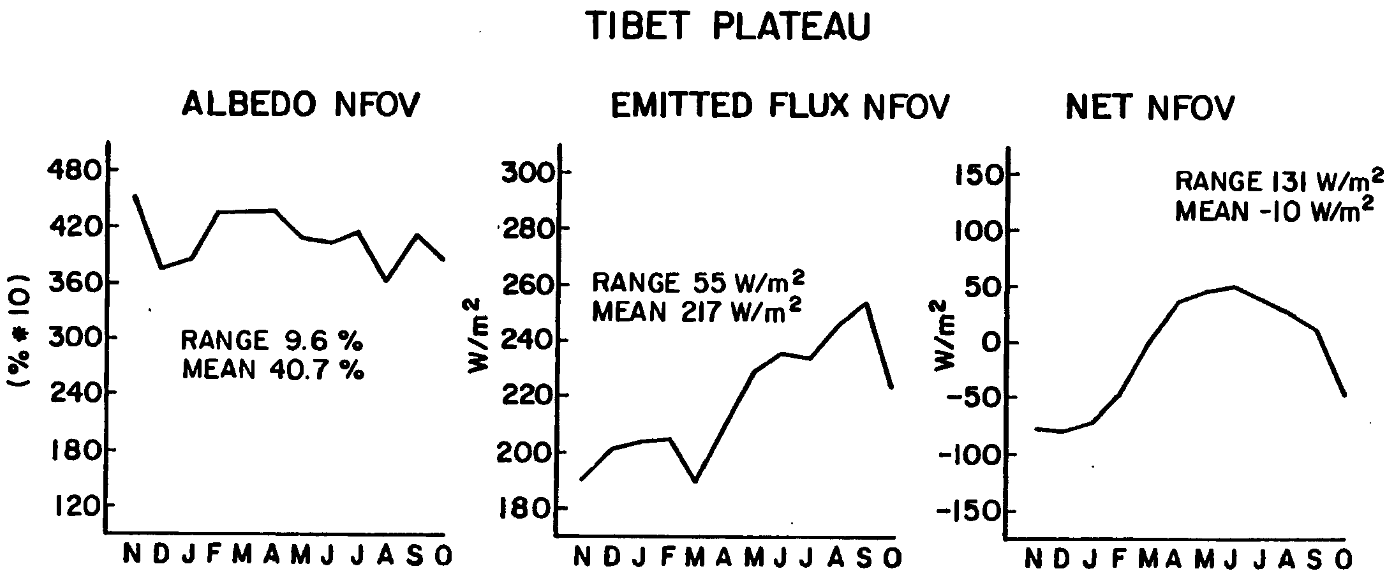

Figure 30. ERB annual cycles Tibet plateau.

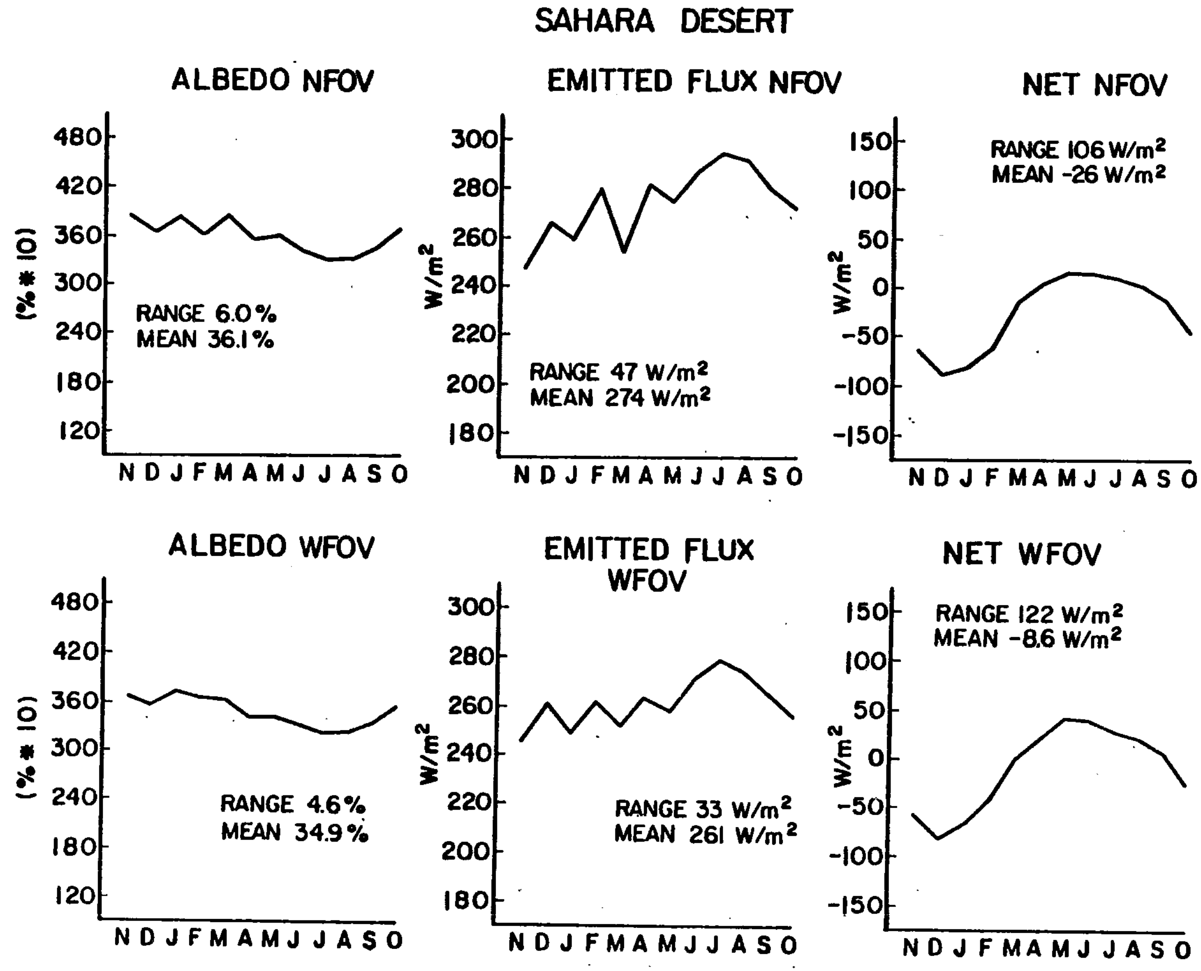

Figure 31. ERB NFOV, WFOV annual cycles Sahara Desert

radiometer was able to sense this smaller scale change as well as the higher gradient that this produced. Throughout this paper this NFOV ability to sense smaller scale features has been noted, but it is the ability to sense the larger gradients produced between cloud and cloud-free regions tha makes the scanner's results important. We are then able to distinguish between adjacent areas that have distinctly different ERB characteristics. The Sahara is exceptionally uniform for such a large continental area, thus the overall WFOV cycles are not unlike that from the NFOV.

The oceanic areas include samples from equatorial, subtropical, and mid-latitude locations. Figure 32 shows the radiation budget of the equatorial Atlantic ocean. With annual variation in the albedo of 7%, the IR flux of 20 W/m^2 and NET of only 34 W/m^2, this is the most stable location that is found anywhere on earth. There is little change in cloudiness due to the constant location of the ITCZ, and the ocean and air temperature remain almost unchanged throughout the year. The whole change in the NET may be caused by the very small Incident cycle which varies only 44 W/m^2 annually. The two period cycle characteristic of the tropics can be seen in all the radiation budget cycles. Pacific ITCZ locations show similar patterns, but equatorial Indian Ocean areas do not. The cross equatorial flows that develop here during the monsoon months shift the location of the ITCZ well away from the equator.

Off the west coast of South America between 9° and 22°S, strong cold water upwelling is found. This is caused by divergence away from the coast of surface water in the Peru current. This colder ocean water and subtropical subsidence keeps this area, as well as most subtropical areas off the west coast of continents, cumulus convection free.

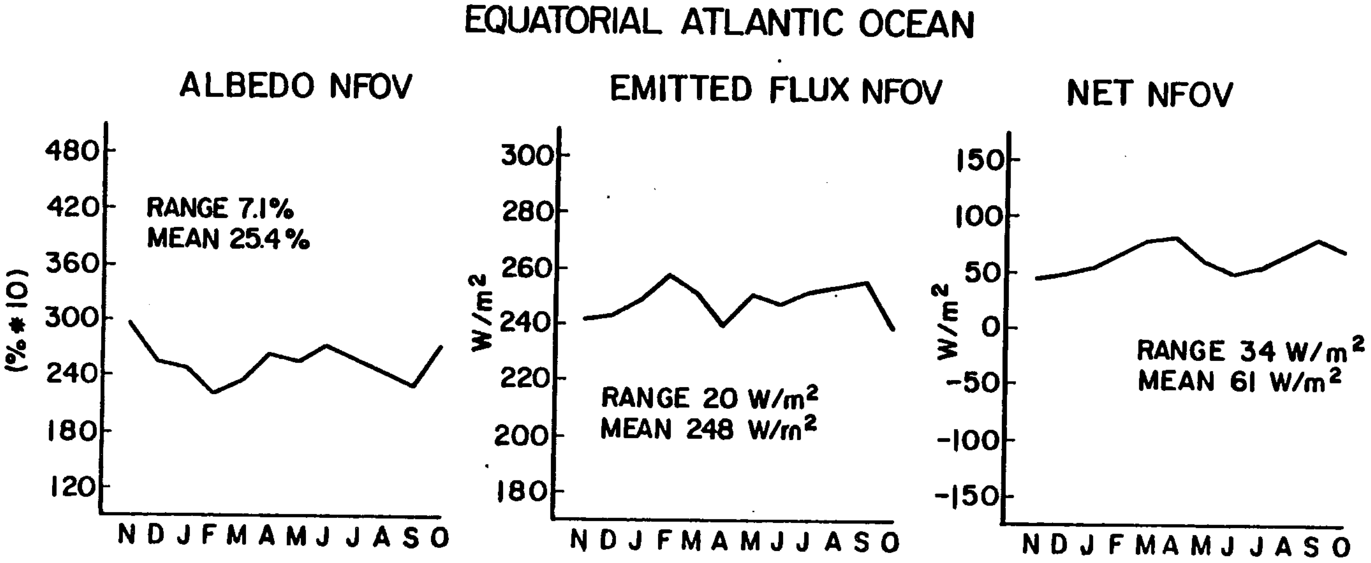

Figure 32. NFOV ERB cycles for Equatorial Atlantic Ocean.

Present are constant low stratocumulus that emit at near surface temperature. Thus even when the statocumulus clouds dissipate, changing the albedo, the IR flux shows very little variation. This is shown by the radiation budget of the area off South America, Figure 33. The albedo shows an annual change of 16%, but the change in the IR flux of only 10 W/m^2 is the lowest annual variation found. The NET actually varies by more than the incident radiation due to the effect of the albedo change. The IR flux shows random variation throughout the year, but the amplitude is so small any surface temperature variation from changes in the cold upwelling or cloud cover could be the cause.

Moving further from the equator we find the regions of maximum variation in the NET radiation. These are oceanic areas roughly at 40-45° latitude off the east coast of continents. These show very low variation in albedo due to the lack of summer convection. The area presented in Figure 34 is from the east coast of Australia to New Zealand. A change of 17% is found in the albedo with the IR flux variation of only 22 W/m^2. This area, as well as all at this latitude, have a high variation of incident radiation (384 W/m^2), and with small changes in the albedo and IR flux the NET variation is accordingly high at 274 W/m^2. Northern Hemisphere oceans have a higher variation in the emitted flux, because in summer continental heating effects cause warmer zonal air temperatures. Higher emitted flux occurs during the time of maximum incident radiation thus decreasing the maximum in the NET radiation. ERB data with the first harmonic removed is plotted to show what variations are apparent outisde of the annual cycle. The decreases of albedo in January and April, as well as the increase in IR flux in these months stand out as the dominate anomalous features.

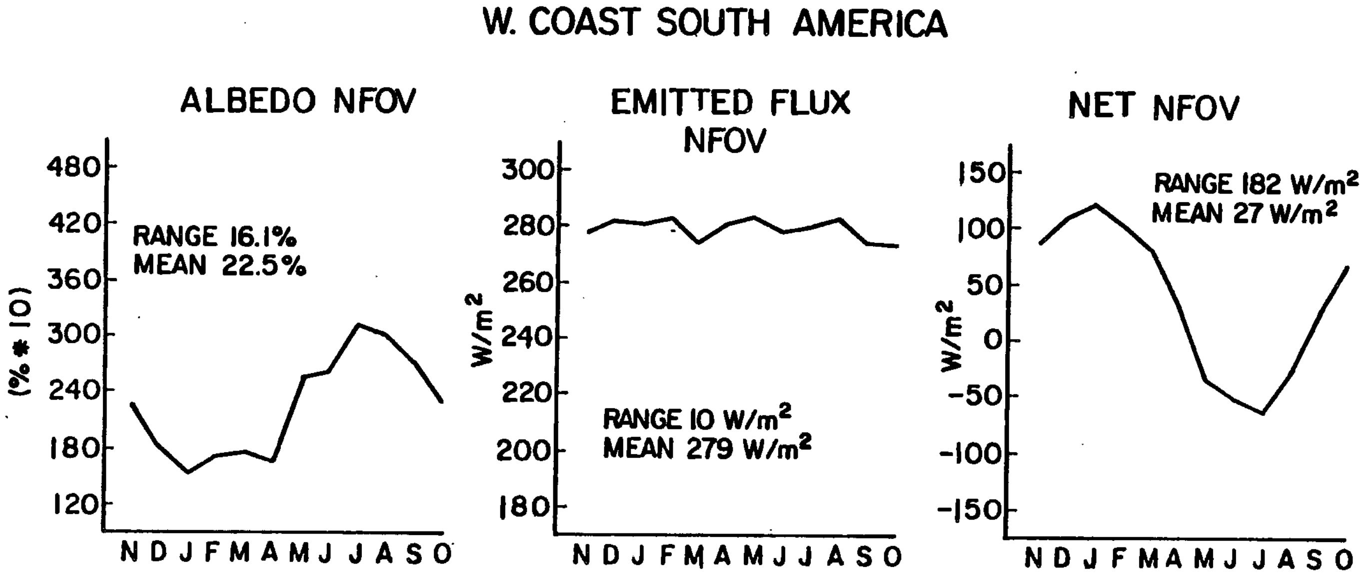

Figure 33. NFOV ERB cycles for Pacific Ocean off the West Coast of South America.

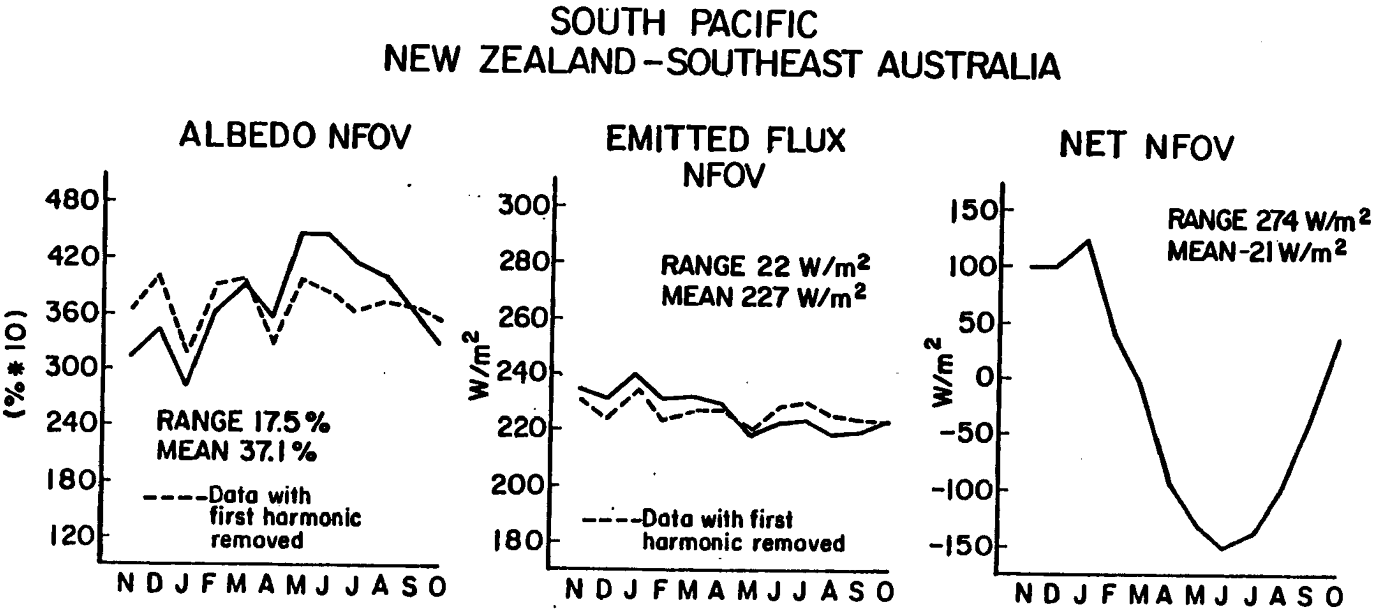

Figure 34. NFOV ERB cycles for the South Pacific between New Zealand and Australia.

The last of the six areas shows some of the most unique ERB changes found anywhere. The Bay of Bengal, Figure 35, shows what changes an area under monsoon influence can exhibit, and is an excellent example of an area totally dominated by cloud effects. There are many WFOV versus NFOV differences therefore the WFOV data is also presented. In May at the onset of the monsoon, the albedo increases dramatically and the IR flux drops. The NFOV shows a 18.4% albedo rise while the WFOV shows only 4.2%, and the NFOV IR flux accordingly drops by 58 W/m^2 compared to 21 W/m^2. These differences cause a reversal in sign of the NET radiation change for the month. The NFOV NET decreases 26 W/m^2 while the WFOV increases by 4.1 W/m^2. During this month the Burma monsoon has taken effect causing only small convection and as yet not any major tropical storms as are found in mid-summer. Due to these large NFOV, WFOV differences, future studies will attempt to find out if variations in certain cloud type or amount could be the cause. This area actually shows moderate annual change in NET radiation, but due to monsoon cloudiness the albedo varies by 34% and the IR flux by 120 W/m^2. These are the highest variations that were found anywhere in the tropics. The annual cycle of incident radiation is plotted with the NFOV NET in order to show the moderating influence in the summer and fall months caused by the monsoon cloudiness.

3.3.2 Daily

The scanning radiometer has a much improved data population due to its ability to sense areas away from the sub-satellite point. For most days the entire earth is sampled, with as many as 10-15 observations per data point. This makes possible daily output fields of the broadband

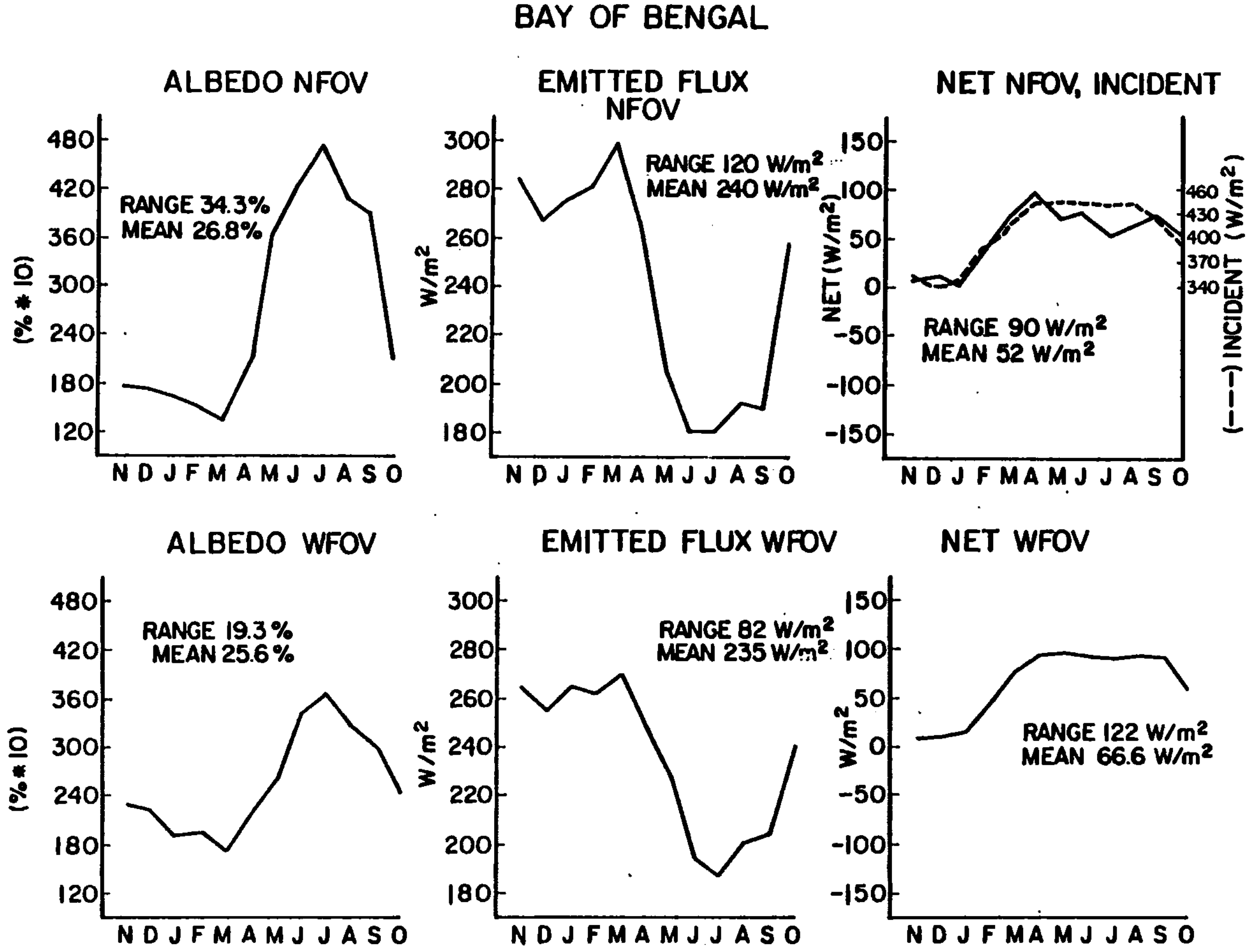

Figure 35. NFOV, WFOV ERB cycles for the Bay of Bengal.

earth radiation budget measurements. In this section, three distinctly different daily situations will be presented. These include a synoptic cyclone system in the North Pacific, the blocking situation of March 21 mentioned earlier, and a look at two hurricanes and the anomalies they created in the ERB.

During the second week of February, a strong cut-off low pressure area formed in the Gulf of Alaska. Figure 36 shows the 700 mb field during this time.

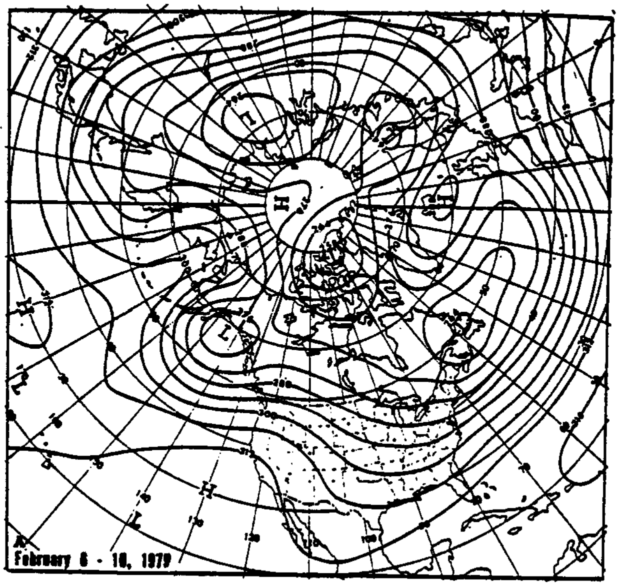

Figure 36. Average weekly 700 mb field, February 6-10, 1979.

By February 10th, the primary surface front associated with this system had come onshore in Oregon and Washington, but the upper air low remained stationary. A second short wave progressed down into the trough forming a second surface cyclone. On the GOES-W satellite image for February 10th, Figure 37, the cyclone is easily seen, as well as the broken clouds in the area of the cut-off Low. ERB data from this day and time are presented in Figures 38 and 39. The effect of the cyclone cloudiness can be seen as an increased albedo and strongly depressed IR

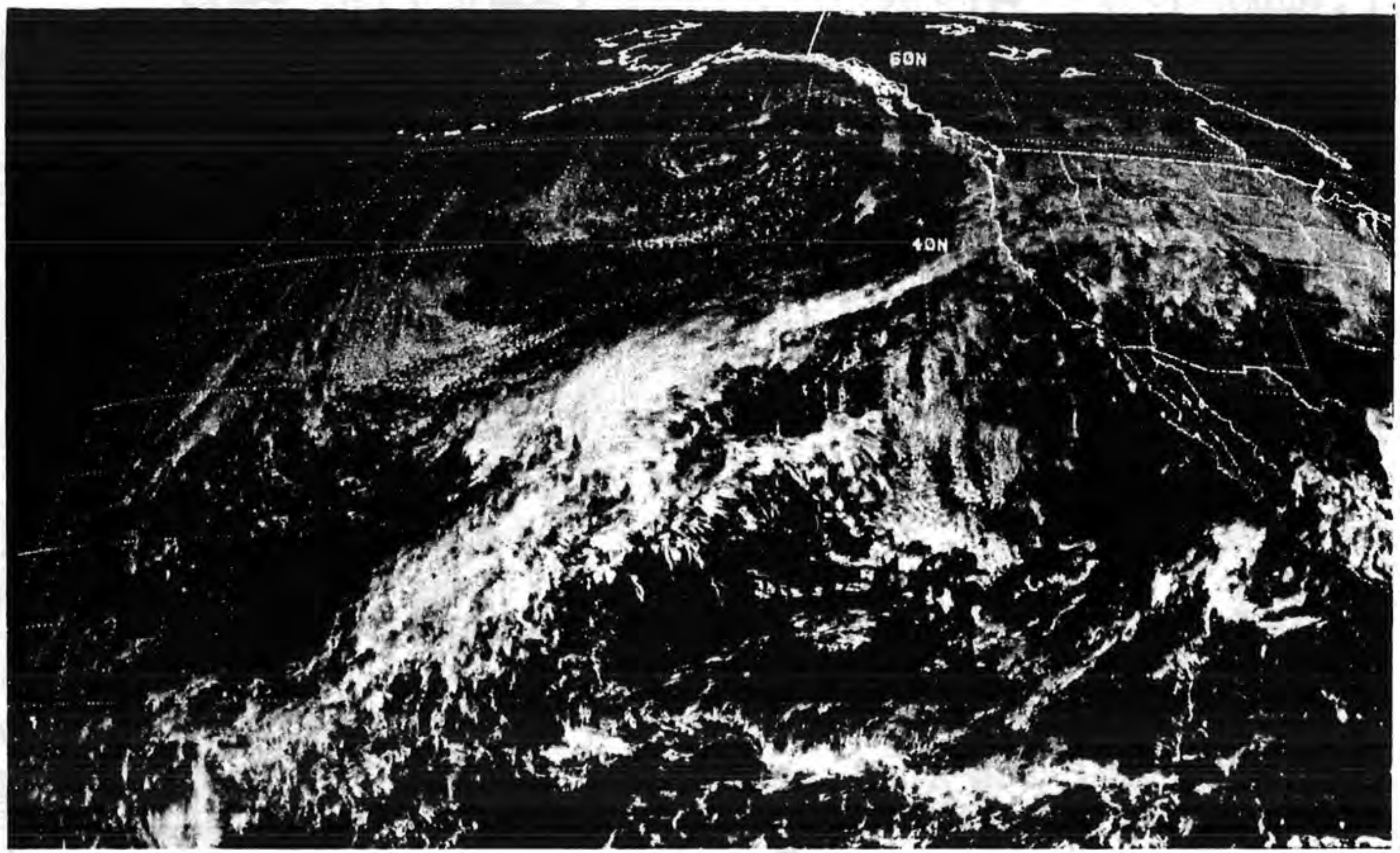

Figure 37. GOES-W visible 2115Z February 10, 1979.

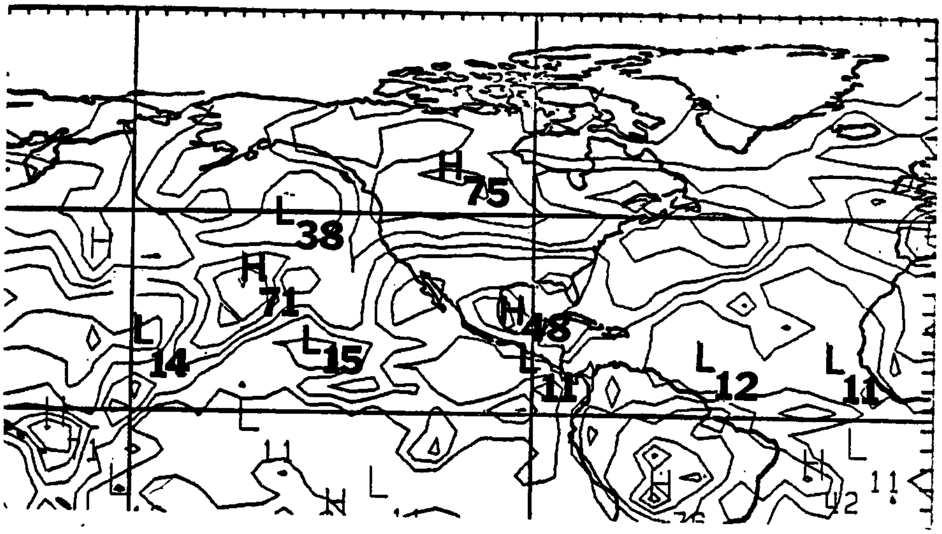

Figure 38. NFOV albedo February 10, 1979 (%)

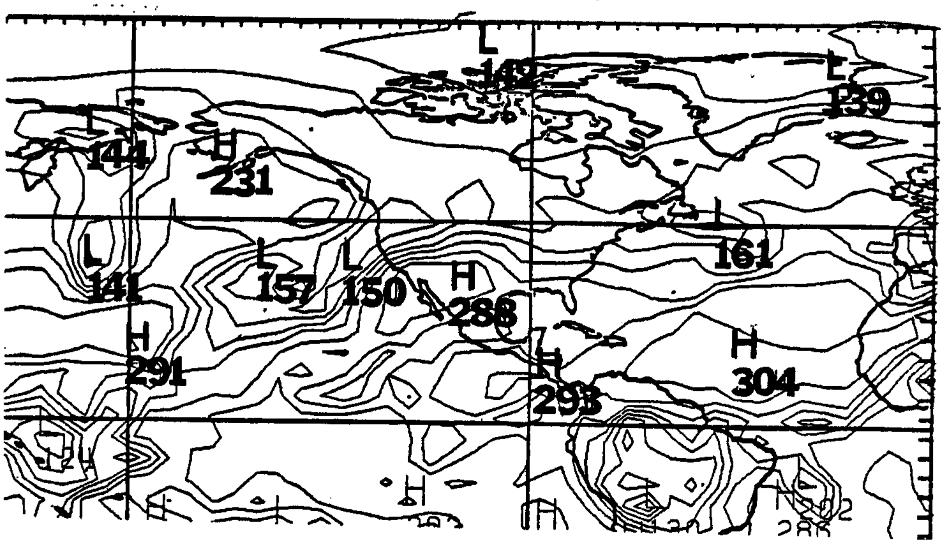

Figure 39. NFOV emitted flux February 10,1979 (W/m^2)

flux. It is important to note what effect this mid-latitude system has on the subtropics. Radiation anomalies trail to the southwest of the synoptic system intersecting with the tropical ITCZ. This is believed caused by the subtropical jet being directed into the developing surface cyclone. One other interesting note, the extremely zonal albedo values across the U.S. located at approximately 35°N are a result of the southern boundry of the snow and ice line.

The average weekly 700 mb field for March 20-24 is shown in Figure 40. March 21 of this week is the day used in the blocking flow versus zonal flow comparison shown in Figures 27-29.

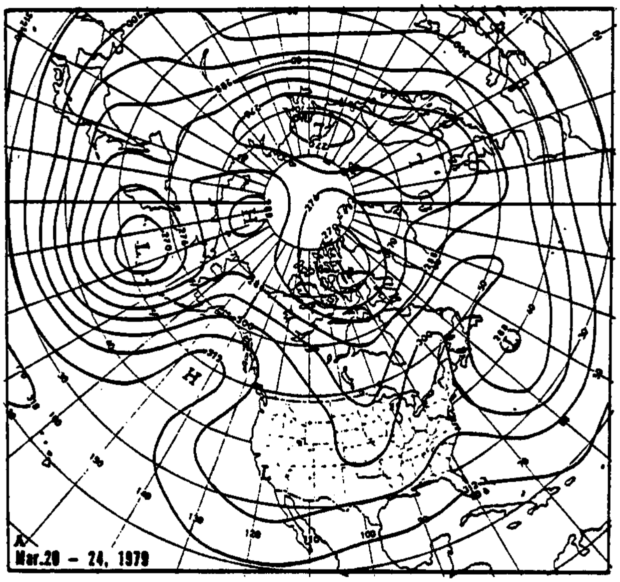

Figure 40. Average weekly 700 mb field, March 20-24, 1979.

For this day there are ridges off the immediate west coast of the U.S. and on the east coast, with major troughs in the central Pacific and central U.S. This situation of deep troughs and steep ridges is called a blocking pattern due to its ability to stop the westerly progression of surface systems. The anomalies created in the ERB for March 21st are shown in Figures 41-43. In the map of emitted flux, much higher values

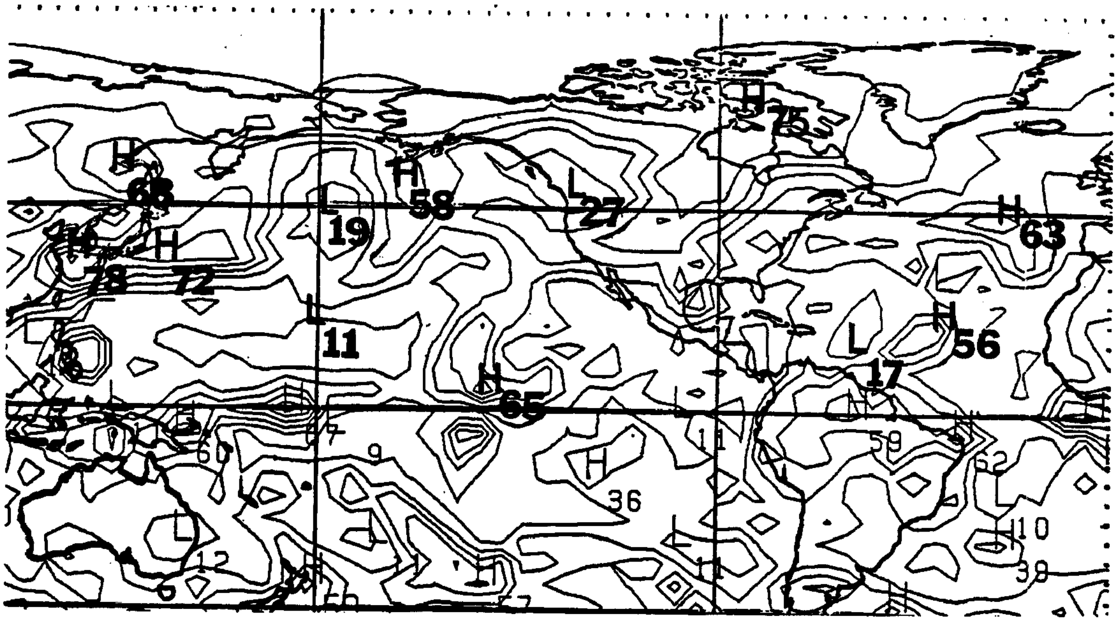

Figure 41. NFOV albedo March 21,1979. (%)

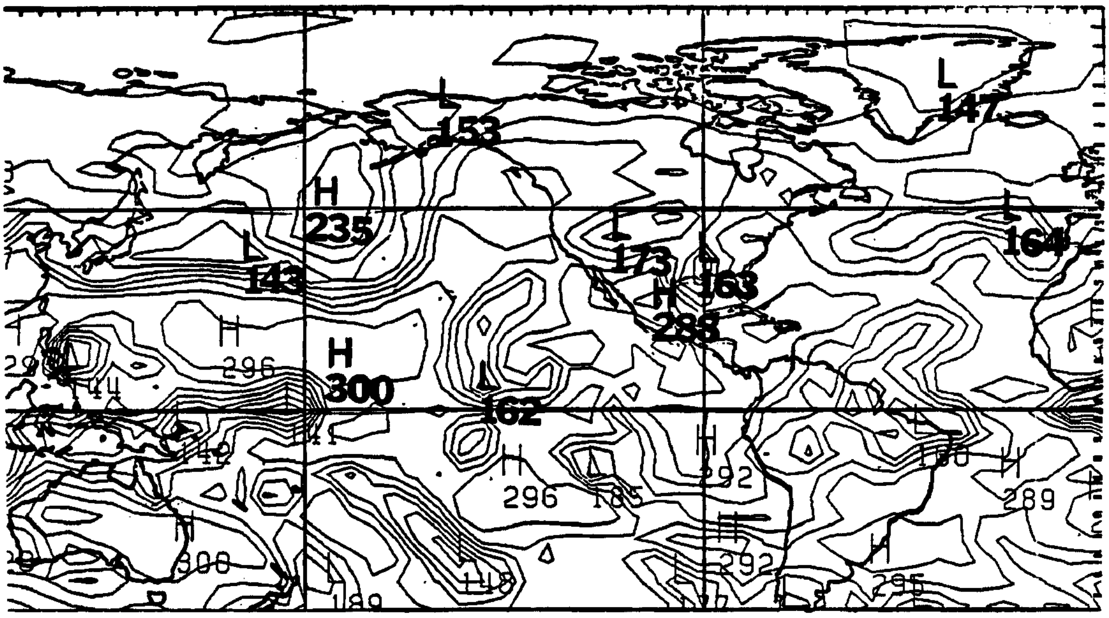

Figure 42. NFOV emitted flux March 21,1979 (W/m^2)

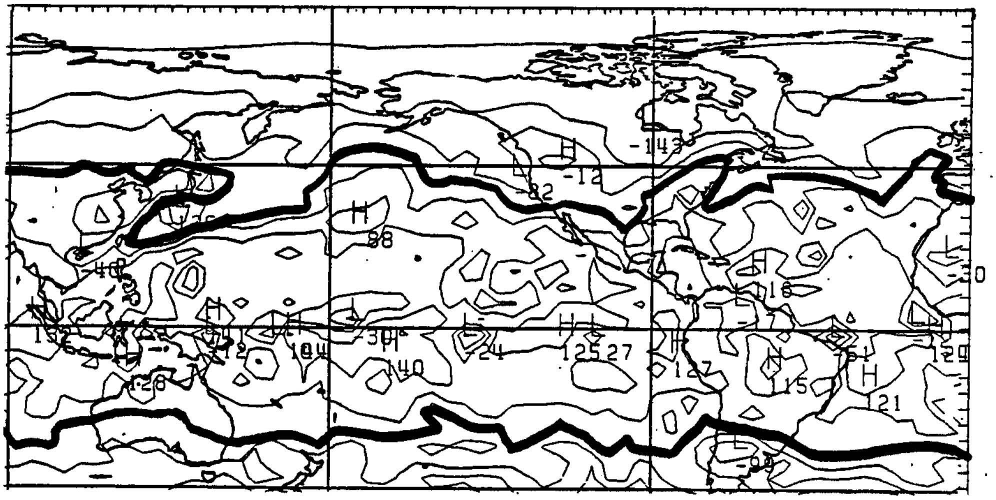

Figure 43. NET radiation March 21, 1979.

are found in the ridges and also in the center of the cut-off mid-Pacific Low. These values clearly indicate the clearer, warmer weather that is associated with major ridges. A synoptic cold front is stacked up against the west side of the Pacific ridge showing higher albedo values and lower IR flux. It is the southwest warm flow that precedes this front that helps build and maintain the ridge. Two areas of low IR flux are present in the central U.S., one centered over the Rocky Mountains due to snow cover, and the other from cumulus convection near the Gulf of Mexico. The NET radiation for this day, Figure 43, shows a very large surplus in the area of the Pacific cut-off Low, but otherwise we see little of the variability shown in the albedo and IR flux maps.

The last of the daily cases occurs on September 2 in the Caribbean Sea. On this day two mature hurricanes, Frederic and David can be located by their associated IR flux minimums shown in Figure 44. David is located off the southeast coast of Florida, and Frederic is still east of the Lesser Antilles. David continued north making landfall in central Florida then progressed into the eastern seaboard states. Frederic moved west along Cuba, intersecting the U.S. coast in Alabama and Mississippi. The high IR flux north of South America indicates a clear region between the two storms. The area of minimum emission off the coast of Louisana is caused by large thunderstorms which are enhanced from the Gulf moisture. These features are easily identified in the 1400Z GOES-E image, Figure 45. The albedo anomalies caused by the hurricanes are shown in Figure 46, where values of over 60% are measured northeast of the hurricane centers. The NET radiation map is not included, but the clear ocean areas show a net gain of 60–120 W/m^2, whereas over the hurricanes a NET loss occurs a greater than 15 W/m^2.

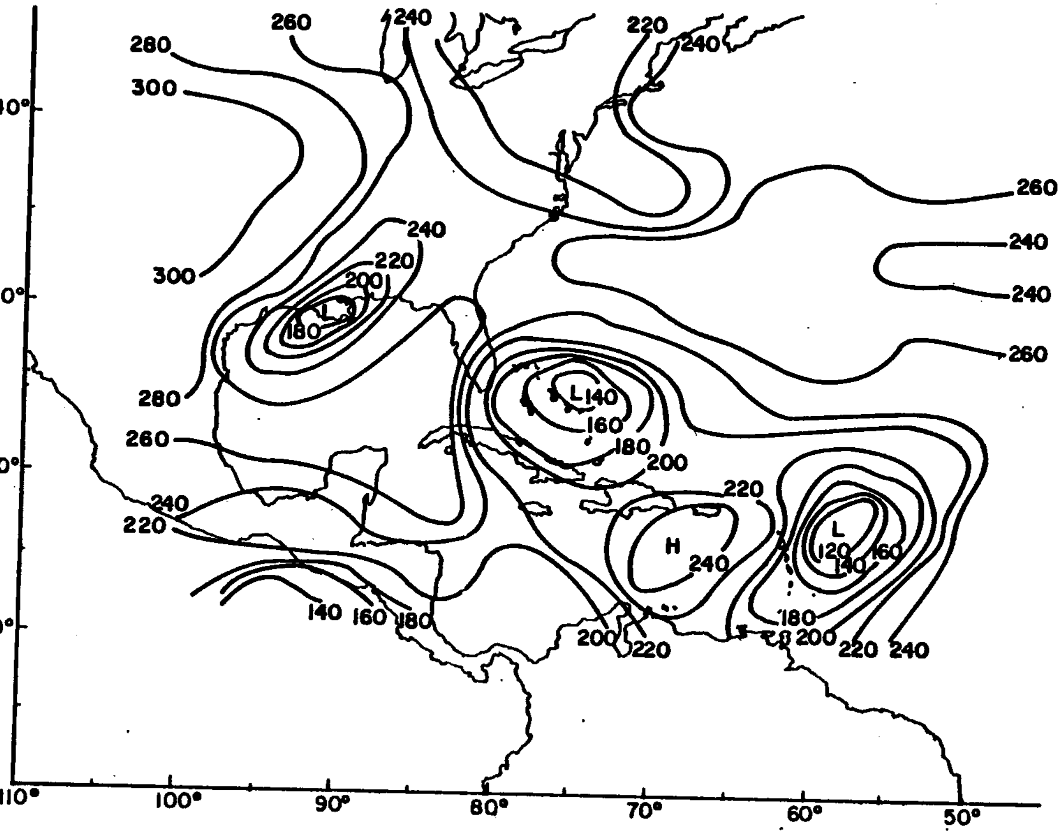

Figure 44. NFOV emitted flux for September 2, 1979.

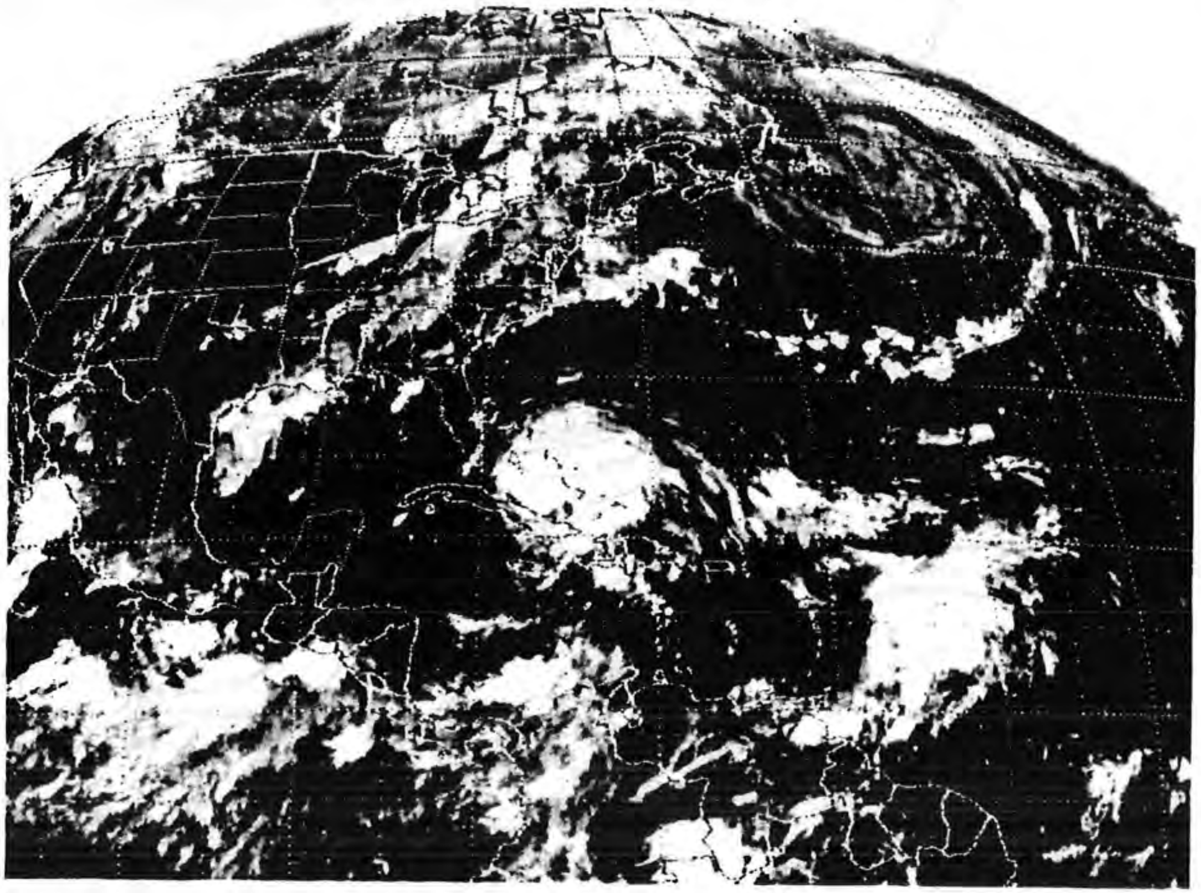

Figure 45. GOES-E IR image 1400Z September 2, 1979.

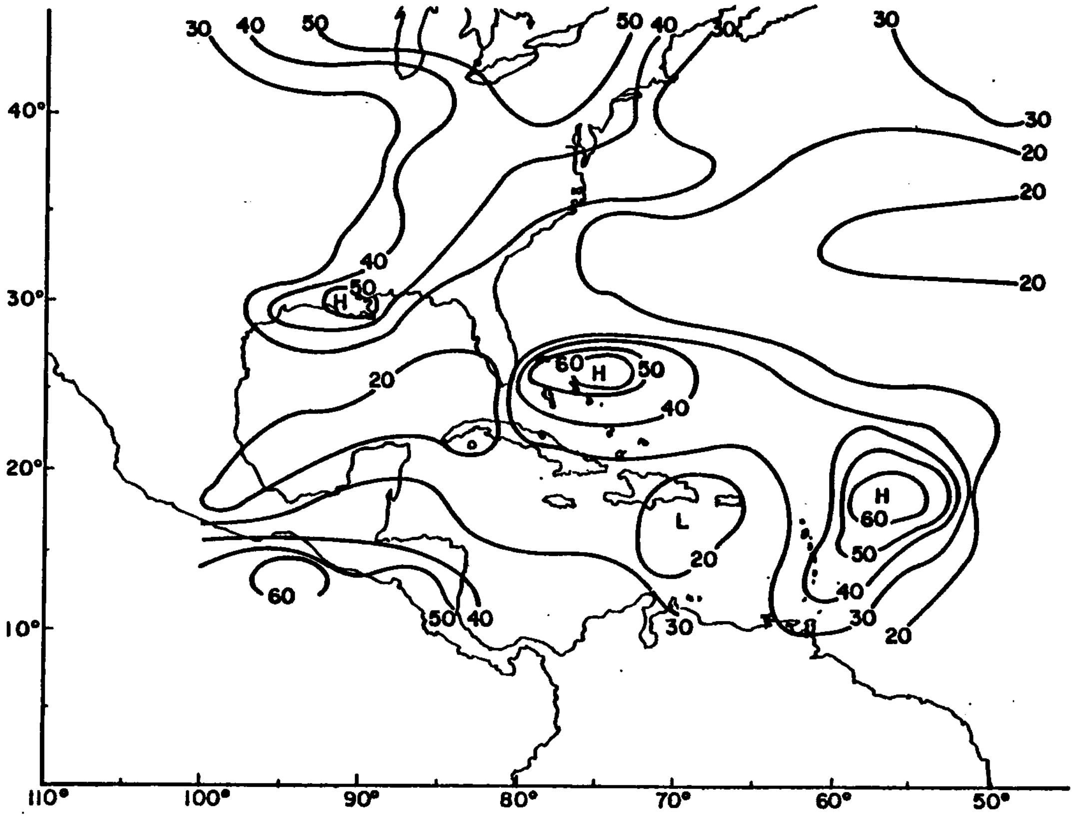

Figure 46. NFOV albedo for September 2, 1979.

To discover if any diurnal changes in the hurricanes could be detected, the daytime (ascending node—AN) data was differenced with the nighttime (descending node—DN) data (Figure 47). The DN pass was 12 hours before the AN pass due to the recording of the data on GMT. Near the hurricane locations the night emissions were measured as much higher. This was originally thought due to a daytime maximum in cloudiness, but actually it is the movement of the hurricanes that brings about this difference. The nightime maximum occurs along the storm track but out in front of the actual hurricane position. These areas have clear skies for high nightime emission, but during the day the hurricane has moved into the area, thus causing the areas to have a much lower emitting temperature. Thus, the values shown in the hurricane locations are actually the change in emitted flux between clear skies and that over the hurricanes. Following the hurricanes in Lagrangian fashion showed 10—20 W/m^2 less emitted flux during the day. This could be caused by a daytime cloudiness maximum or since the night measurement was 12 hours before the day, natural intensification over the period. The other predominate diurnal feature is the large daytime maximum over the central U.S. caused by nocturnal thunderstorms in a severe weather outbreak. The line of thunderstorm are easily seen in Figure 48 the GOES—E IR image for 0600 Z.

These are just three of many different daily situations that could be studied with the scanning radiometer data. It is over this regional scale that results from this instrument can be put to the greatest use.

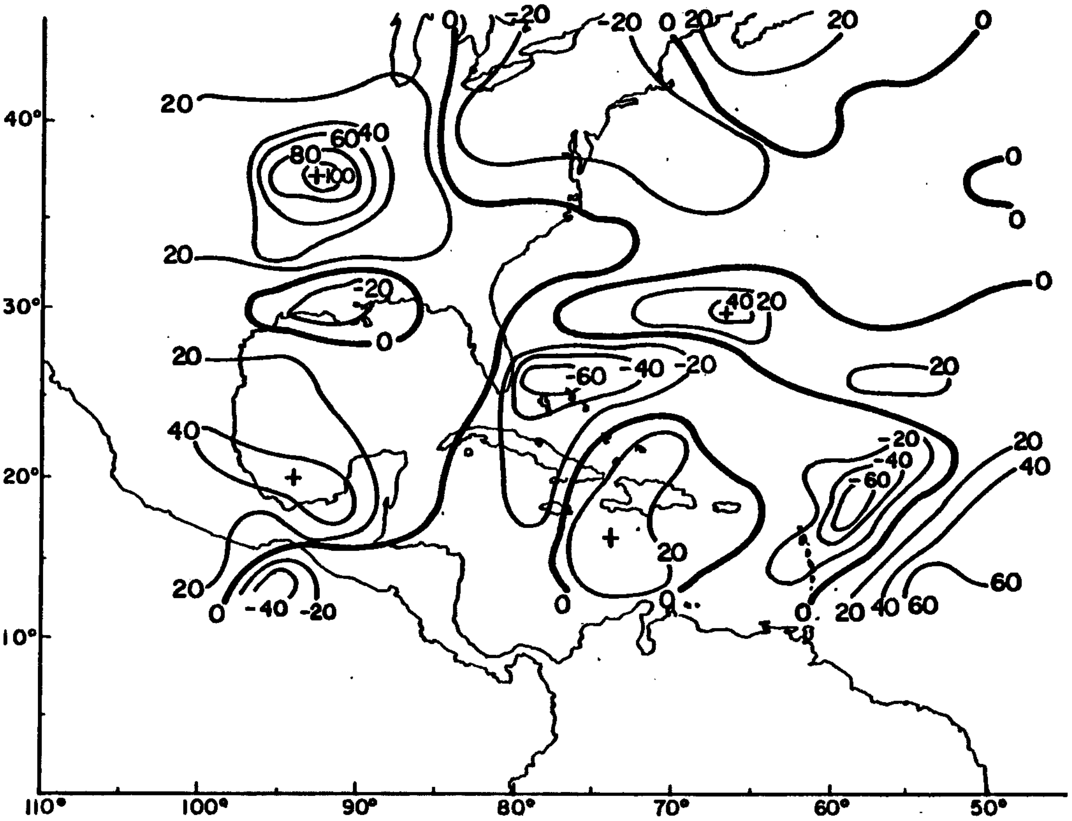

Figure 47. NFOV diurnal emitted flux difference September 2, 1979 positive values are daytime maximums.

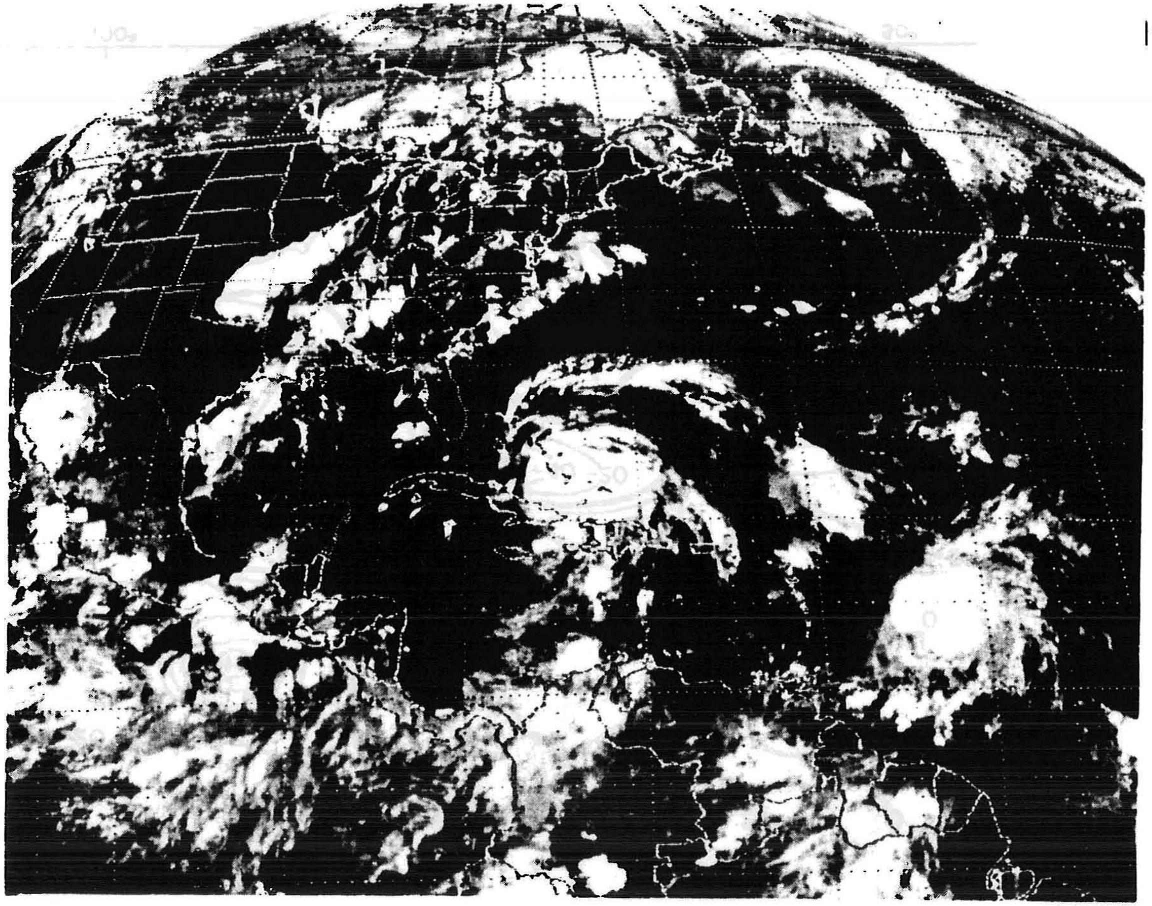

Figure 48. GOES-E IR image 0600Z September 2, 1979.

4.0 Conclusions

Different temporal and spacial scale Earth Radiation Budget (ERB) results from the Nimbus 7 ERB instrument have been presented. The satellite produced measurements from two different sets of instruments, scanning radiometers (NFOV), and fixed hemispheric radiometers (WFOV). The scanning instrument produced higher resolution data, thus smaller scale ERB anomalies created by the ITCZ and other general circulation features could be seen. The NFOV scanner data showed higher albedo in the location of the tropical ITCZ, and lower albedo in the subtropics than the WFOV. Also seen in the NFOV data was less emitted flux in the tropics and larger emitted flux in the subtropics. These differences have the effect of increasing both the albedo and emitted flux gradients between these areas.

The annual range of each NFOV ERB parameter was defined and areas of high and low annual variation pointed out. High albedo variation areas include; areas near the polar night terminator, the tropics effected by the Asian monsoon, and the South Pacific Convergence Zone. Albedo areas having small annual variation include; the Sahara desert and the oceanic subtropical regions off the west coast of continents. Areas of high emitted flux variation are found predominately in the same areas of high albedo variation, and due to seasonal heating effects, over the continents. The NET radiation variation is much more zonal with the tropics having little annual change, the mid-latitudes showing the maximum, and the polar regions having lower values. The annual cycles of six specific areas having high ERB annual variability were examined and the causes for the abnormal variation discussed.

The zonal averaged annual radiation budget for both instruments was presented. Zonal averaged annual range of the ERB parameters was calculated and showed much higher variation in the northern hemisphere (NH). The NH ERB zonal averages were examined during different circulation patterns, a blocking situation, and one of zonal flow. The blocking case caused a decrease in the gradients of albedo and emitted flux in the mid-latitudes as well as strongly decreasing (30-40%) the gradients between the subtropics and tropics. In the future many of these cases will be examined to determine if this was an isolated effect.

The annual cycles of Global averaged albedo, emitted flux and NET radiation were included, with the albedo cycle showing great variation between the two instruments. Finally broadband ERB results on the daily time scale were presented, where it was shown that a synoptic system caused radiation anamolies that reached well out of the mid-latitudes. This was actually a look into what work might be accomplished in the future with this data set.

There are a great number of uses for this Nimbus 7 data set tha were not touched on here. Many more results can be obtained from studying the ERB of regional scale areas. Working with the daily data shows promise for many major projects.

REFERENCES

Burden, R. L., J. D. Faires, A. C. Renolds, 1978: Numerical Analysis Prindle, Weber and Schmidt, Boston, Mass.

Campbell, G. G., 1982: Scanning versus Integrated Sensor Observation of Earth Radiation Budget, a short report sent to the ERBE Measurement Analysis Working Group, personal communication.

Campbell, G. G. and T. H. Vonder Haar, 1980: An analysis of two years of Nimbus 6 Earth Radiation Budget observations: July 1975 to June 1977, Department of Atmospheric Science, Colorado State University, Fort Collins, Colo, Atmospheric Science Paper 320.

Charney, J. G., 1975: Dynamics of Deserts and Drought in the Sahel Quarterly Journal or the Royal Meteorological Society, Vol. 101, No. 428, April 1975, pp 193-202.

Durkee, P., E. Hindman, and T. H. Vonder Haar: On the use of the Nimbus 7 CZCS for Marine Aerosol Characterization. In preparation for submission to Journal of Geophysical Research.

Earth Radiation Budget tape documentation, 1981. Requirements document NG #10 Revision F, Systems and Applied Science Corporation.

Earth Radiation Budget Science 1978 proceedings of a workshop held at Williamsburg, Virginia, March 28-30, 1978, NASA Conference publication 2100, pp. 72.

Ellis, J. S., T. H. Vonder Haar, S. Levitus, and A. H. Oort, 1978: The annual variation in the global heat balance of the earth. J. Geophys. Res., 84, 1958-1962.

Ellis, J. S. and T. H. Vonder Haar, 1976: Zonal average earth radiation budget measurements from satellites for climate studies, Atmospheric Science Paper 240, Colorado State University, Fort Collins, Colo.

Gruber, A., and J. S. Winston, 1978: Earth-Atmosphere radiative heating based on NOAA scanning radiometer measurements. Bull. Am. Meteorol. Sci., 59, 1570-1573.

Hickey, J. R., B. M. Alton, F. J. Griffen, H. Jacobowitz, P. Pellegrino, R. Maschoff, E. A. Smith, and T. H. Vonder Haar, 1981: Extraterrestrial Solar irradiance variability: two and one half years of measurements from Nimbus 7 (accepted for publication in Solar Energy, 1982).

Holton, J. R., 1972: An Introduction to Dynamic Meteorology, Academic Press, New York.

House, F. B., 1965: The radiation balance of the earth from a satellite. Ph.D. thesis, Department of Meteorology, University of Wisconsin, 69 pp.

Jacobowitz, H., H. V. Soule, H. L. Kyle, F. House, Nimbus 7 ERB Experiment Team, 1983: The Earth Radiation Budget (ERB) Experiment An Overview. Submitted to J. Geo. Res.

Jacobowitz, H., L. L. Stowe and J. R. Hickey, 1978: The Earth Radiation Budget Experiment, the Nimbus-7 User's Guide, NASA Goddard Space Flight Center, Greenbelt, MD, pp 33-69.

London, J. and T. Sasamori, 1971: Radiative Energy budget of the Atmosphere Space Research XIII, Amsterdam, North Holland, Pub. Co.

London, J., 1957: A study of the atmospheric balance. Final Report Contract AF19(122)-165, Department of Meteorology and Oceanography, New York University, 99 pp.

Raschke, E., T. H. Vonder Haar, W. R. Bandeen and M. Pasternak, 1973: The annual radiation balance of the earth-atmopshere system during 1969-1970 from Nimbus 3 measurements, J. Atmos. Sci., 30, 341-364.

Raschke, E., and W. R. Bandeen, 1970: The radiation budget of the planet Earth from radiation measurements of the satellite Nimbus 2, J. Appl. Meteorol., 9, 215-238.

Sellers, W. D., 1965: Physical Climatology. The University of Chicago Press, Chicago, Ill.

Stephens, G. L., G. G. Campbell, and T. H. Vonder Haar, 1981: Earth Radiation Budgets, J. Geophys, Res., 86, 9739-9760.

Vemury, S. K., L. Stowe, H. Jacobowitz, 1983: Sample size and scene identification (cloud): Effect on albedo. Submitted to the Journal of Geosphysical Research.

Vonder Haar, T. H., 1981: Semi-Annual Report to the NASA Langley Research Center - Radiation Budget Measurement/Model Interface Research.

Vonder Haar, T. H., G. G. Campbell, E. A. Smith, A. Arking, K. Coulson, J. Hickey, A. Ingersoll, H. Jacobowitz, L. Smith and L. Stowe, 1981: Measurements of the Earth Radiation Budget from satellites during the first GARP global experiment. Adv. Space Res., 1, 285-297.

Vonder Haar, T. H., and J. Ellis, 1977: The Annual Cycle in Planetary Radiation Exchange with Space. Radiation in the Atmosphere Science Press.

Vonder Haar, T. H., 1972: Natural variation of the radiation budget of the earth-atmosphere system of measured from satellites (conference on Atmospheric Radiation, August 7-9, 1972, Fort Collins, Colo.) published by AMS, Boston, Mass.

Vonder Haar, T. H., and V. E. Suomi, 1971: Measurements of the Earth's Radiation Budget from satellites during a five-year period. Part 1: Extended time and space means. J. Atmos. Sci., 28, 305-314.

Vonder Haar, T. H., 1968: Variation of the earth's radiation budget. Ph.D. dessertation, Department of Meteorology, University of Wisconsin, 118 pp.

Wallace, J. M. and P. V. Hobbs, 1977: Atmospheric Science: An Introductory Survey. New York Academic Press.

Winston, J. S., and V. R. Taylor, 1967: Atlas of world maps of longwave radiation and albedo for seasons and months based on measurements from TIROS IV and TIROS VII. ESSA Tech. Report, NESC, 43, 32 pp.